*buildings*

MDPI

*Article*

# A Novel Solar Rooftop Agriculture System Integrated with CNT Nanofluid Spectral Splitter for Efficient Food Production

**Wei Wei [1,†], Jiayi Luo [1,†], Yiyu Shi [1], Chenlei Yu [1], Niansi Li [1,2], Jie Ji [2] and Bendong Yu [1,*]**

[1] College of Urban Construction, Nanjing Tech University, Nanjing 210009, China; wwfyynitech@163.com (W.W.); 202221134050@njtech.edu.cn (J.L.); syy031013@163.com (Y.S.); yuclbetty1010@163.com (C.Y.); liniansi@njtech.edu.cn (N.L.)

[2] Department of Thermal Science and Energy Engineering, University of Science and Technology of China, Hefei 230026, China; jijie@ustc.edu.cn

* Correspondence: yubendonglns@163.com

† These authors contribute equally to this work.

**Abstract:** Traditional rooftop greenhouses offer a promising solution for urban vegetable supply but have the disadvantages of overheating during the daytime and supercooling during the nighttime. To address these issues, a novel solar greenhouse system using nanofluid spectral splitting and phase change materials (NSS-PCMs) was developed. In this study, a 75-day thermal environment test experiment was conducted on the novel solar greenhouse, and the growth status and nutrient composition of three typical plants were evaluated. By optimizing the greenhouse structure parameters through the model, over 80% of 300–800 nm wavelengths for vegetable photosynthesis were transmitted to the greenhouse, while the remaining spectrum was used for heat storage to maintain warmth during nighttime. The novel solar greenhouse reduced daytime temperatures by 5.2 °C and increased nighttime temperatures by 6.9 °C, reaching a maximum thermal efficiency of 53.4% compared to traditional greenhouses. The 75-day temperature detection showed that optimal temperature ranges were maintained for approximately 60 days, both during daytime and nighttime, with an 80% assurance rate. The growth rates of three vegetables in the novel solar greenhouse improved by 55%, 35%, and 40%, and the nutrient composition doubled compared to the control group.

**Keywords:** rooftop agriculture; spectral splitting; nanofluid; phase change material; solar energy



Academic Editor: Adrian Pitts

Received: 24 December 2024
Revised: 18 January 2025
Accepted: 20 January 2025
Published: 21 January 2025

**Citation:** Wei, W.; Luo, J.; Shi, Y.; Yu, C.; Li, N.; Ji, J.; Yu, B. A Novel Solar Rooftop Agriculture System Integrated with CNT Nanofluid Spectral Splitter for Efficient Food Production. *Buildings* **2025**, *15*, 314. https://doi.org/10.3390/buildings15030314



## 1. Introduction

Global population growth and rapid urbanization are putting pressure on food security, a problem made even more acute by the rising demand for food [1–3]. In the urban environment, the reduction in vegetable cultivation has become a serious problem. Rooftop agriculture often has better light, and the use of rooftops can meet different personalized planting needs [4]. Rooftop agriculture is not only in line with the development goals of green cities but also plays a role in beautifying and developing more environmentally friendly and low-carbon urban settings [5–7].

Urban agriculture is increasingly gaining attention, as evidenced by the growth of local food production projects [8–10]. The current urban agricultural system showcases a rich diversity, encompassing various methods, models, scales, directions, and objectives, and can flexibly adapt to urban and peri-urban environments [11,12]. Within urban settings, the types of urban agriculture can be classified in various ways based on different production

purposes, market positioning, or technological approaches [13]. Transforming unused balconies into productive spaces is recognized as an effective sustainable development strategy, a view supported by researchers and urban planners. Rooftop agriculture is a facility specifically designed for planting and protecting plants; it provides warmth, ample sunlight, and suitable humidity, which can effectively extend the growing season and enhance growth efficiency.

Traditional solar agriculture is a combination of solar power generation, modern agricultural planting, and efficient facility agriculture [14,15]. The advantage of traditional solar agriculture is that it can convert sunlight into electricity to save energy. The biggest drawback of traditional solar agriculture is that light and temperature are affected by factors such as the economy, region, and climate [16], which might cause plant growth to be hindered or the yield to decline. Additionally, in the cold season, the heat loss may be more significant during nighttime. If there are not enough heat preservation measures, the temperature may decline rapidly during nighttime, affecting the growth of plants [17]. In order to maintain a suitable temperature, traditional solar agriculture requires a lot of heating. This can lead to high energy costs. Therefore, there is an urgent need to design a structure that can be used to provide controllable temperature, light, and other climatic factors so that plants can grow under non-ideal natural conditions. Enhancing the design of conventional solar greenhouses can lessen the environmental effects on agriculture [18], thereby improving land use efficiency and reducing the use of water and pesticides [19,20].

In greenhouse cultivation systems, temperature control is a key factor influencing crop growth and yield. Crops in different climate zones have different temperature requirements. For example, in temperate climates, lettuce grows best at 15–20 °C [21]; in tropical climates, chili peppers grow best at 25–30 °C [22]; tomatoes are most suitable for growth in temperate climates with an ideal temperature of 20–25 °C [23]; and in subarctic climates, carrots grow best at 15–18 °C [24]. Therefore, the temperature is typically controlled between 15 °C and 30 °C, which meets the growth requirements of most common vegetables and fruits. Precise temperature regulation helps improve crop growth efficiency, yield, and quality, especially in greenhouse systems, where temperature can be adjusted based on the characteristics of different climate zones to suit the needs of various crops.

The spectrum required for normal plant growth is 300–800 nm [16], and the temperature is 15–30 °C. Therefore, in order to promote the normal growth of plants, a novel system that can provide appropriate light and spectrum while maintaining appropriate temperature conditions is needed. Reasonable regulation of these factors can help plants make full use of light energy for photosynthesis and maintain normal growth and development. Nanofluids (NFs), recognized as an innovative heat transfer medium with excellent thermal performance, hold significant promise for application in heat transfer systems [25–27]. Nanofluids not only improve the heat transfer efficiency and thermal conductivity [28,29] but also show better light absorption performance [30,31]. Research has demonstrated that CNT/Ag nanofluids have high transmittance at 300–700 nm.

The nanofluid spectral splitting technology involves the introduction of nanoparticles into fluids to selectively absorb and scatter sunlight at specific wavelengths, optimizing heat distribution and improving energy efficiency [32,33]. This technology enhances the solar radiation absorption in the desired wavelength range, reducing excess heat buildup while maintaining a stable temperature within the greenhouse. The use of nanofluids allows for better control of the thermal environment, leading to more efficient energy use and promoting better plant growth [34].

Phase change materials (PCMs) are capable of latent heat thermal energy storage (LHTES) and represent an innovative solution for thermal energy storage (TES) to address global energy demands [35,36]. Several studies have explored various PCM systems to

fulfill the heat requirements of greenhouses. For instance, Benli and Durmuş [37] tested an experimental setup featuring ten solar air collectors integrated with a latent heat storage system. Their results indicated that the temperature inside the greenhouse was 6–9 °C higher than the outdoor temperature due to the size of the integrated PCM collectors. Similarly, Bobadilla et al. [38] incorporated a solar air heater with PCM storage into a small church-shaped greenhouse during winter, resulting in an internal temperature that was 5 °C warmer than the ambient temperature. The collector successfully stored approximately 56% of the waste heat generated during the day, meeting 30% of the nighttime heating demand. However, to date, researchers have not combined the NSS system with PCM and greenhouses.

To address these issues, a novel solar greenhouse system based on nanofluid spectral splitting and phase change materials (NSS-PCMs) was developed for rooftop agriculture. This system leverages nanofluid spectral splitting and PCM to enhance comprehensive solar energy utilization, improve full-spectrum solar efficiency, boost vegetable production efficiency, and save energy. In this study, a 75-day thermal environment test experiment was conducted, and the growth status and nutrient composition of three typical plants were evaluated. The system was first designed and subjected to thermal and spectral experiments. Then, a thermal model was developed and validated, followed by system parameter optimization based on the model. In addition, the thermal performance of the NSS-PCM system was evaluated in comparison to a traditional system. Finally, purslane, asparagus, and lettuce were selected for planting and testing for 75 days. Upon maturity, their growth conditions and nutrient content were measured and evaluated.

The innovative aspect of this study lies in the integration of nanofluid spectral splitting with phase change materials (PCMs) in the development of a novel solar greenhouse system. This system combines the precise thermal regulation provided by nanofluids with the thermal storage capability of PCMs, which absorb excess heat during the day and release it at night, thus stabilizing temperature fluctuations within the greenhouse. This dual approach significantly improves the thermal performance of the greenhouse while also enhancing energy efficiency and plant growth conditions, representing a novel solution compared to traditional temperature control methods.

## 2. Description of Solar Greenhouse with NSS-PCMs

The schematic of the novel solar greenhouse with the NSS-PCM system is depicted in Figure 1. The NSS-PCM system is mainly composed of acrylic glass, nanofluids, PCMs, a serpentine copper tube, a water pump, a heat storage tank, and an aluminum groove, respectively. The nanofluid spectral splitting (NSS) receiver transmits the effective spectrum of plant photosynthesis (300–800 nm) for the growth of plants while absorbing the remaining spectrum of sunlight (800–1500 nm) to generate heat [16]. The nanofluids flow in a channel composed of two glass plates. The PCMs are placed in the aluminum groove on the back of the NSS-PCM system for storing heat to warm the greenhouse during nighttime. Nanofluids not only transmit the plant photosynthesis active spectrum required by plants for plant growth but also absorb the rest of the spectrum of sunlight. Organic paraffin acts as the PCM. The serpentine copper tube is placed in the middle of the PCMs. The nanofluids absorb heat and flow into the copper tube to heat the PCMs for heat storage. PCMs release the heat to warm the greenhouse to maintain an appropriate temperature for the plants and promote plant growth during nighttime. The heat storage water tank plays a role in heat preservation during the day.

During the daytime, the pump is activated, circulating nanofluids from the water tank. These nanofluids effectively absorb solar radiation in the 800–1500 nm spectrum range, causing their temperature to rise quickly. Heated nanofluids then flow into a copper

tube, transferring heat to the phase change materials (PCMs). The PCMs receive this heat, gradually raising their temperature until reaching the phase change point, thereby storing substantial thermal energy. At the same time, any unabsorbed radiation passes directly into the greenhouse, providing essential light for plant photosynthesis and directly warming the greenhouse space. The spectral splitting properties of the nanofluids filter out unnecessary radiation, preventing the greenhouse from overheating and maintaining a stable temperature environment that supports efficient photosynthesis (Figure 2a).

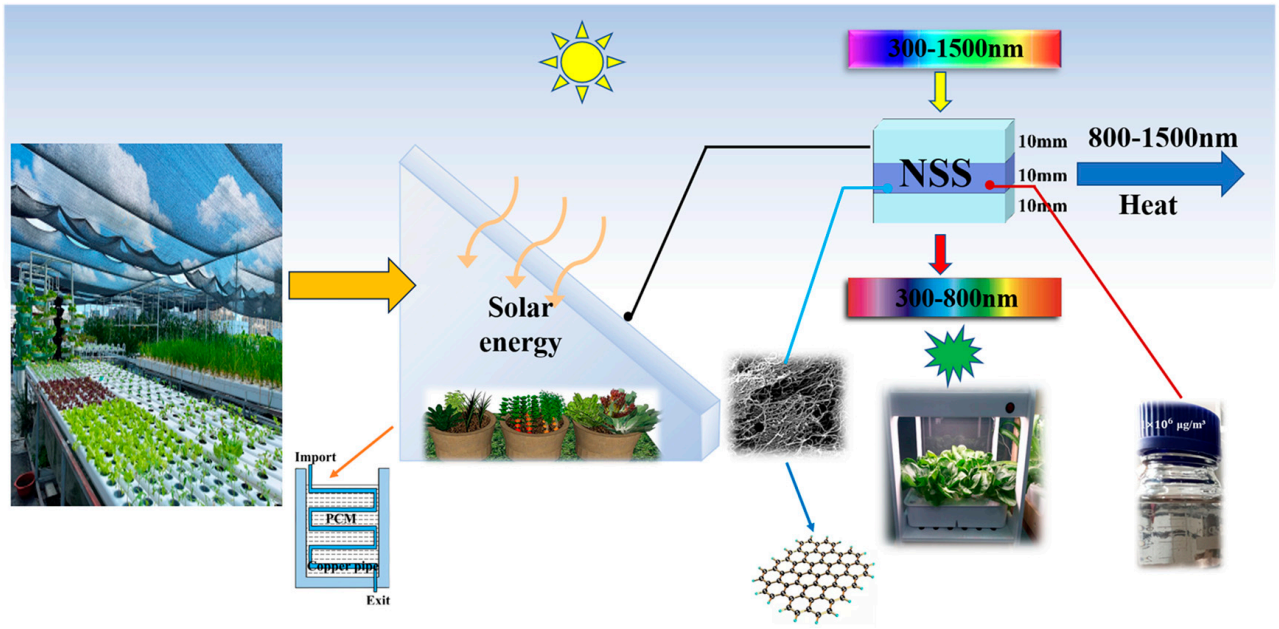


**Figure 1.** The concept and structure diagram of a solar greenhouse with NSS-PCMs.

At night, the system automatically shuts off the pump, returning nanofluids to the water tank and pausing circulation. Meanwhile, the PCMs begin releasing the thermal energy stored during the day, gradually dispersing heat into the greenhouse. This slow heat release by the PCMs effectively slows the temperature drop within the greenhouse, ensuring that the nighttime temperature remains within 15–18 °C. This temperature range is crucial for healthy plant growth, preventing growth inhibition or potential frost damage due to sudden nighttime temperature drops. By releasing and regulating heat in this way, the greenhouse environment remains stable throughout the night, ensuring that plants can maintain their metabolic functions and basic growth needs even without sunlight (Figure 2b).

When comparing a solar greenhouse equipped with a phase change material (PCM) to one without PCM, significant temperature differences are observed during both daytime and nighttime. During the daytime, the interior temperature of the greenhouse with PCM is lower than that of the outside environment, effectively controlling the temperature and reducing heat stress on the plants. In contrast, the greenhouse without PCM experiences higher internal temperatures, which leads to potential heat stress affecting plant growth (Figure 2c).

At night, the PCM system maintains higher internal temperatures by releasing the heat stored during the day, preventing damage to plants due to low temperatures. However, in the greenhouse without PCM, nighttime temperatures drop rapidly, inhibiting plant growth and possibly causing frost damage. This comparison demonstrates that the greenhouse equipped with PCM has a clear advantage in temperature regulation and in protecting plant growth (Figure 2d).

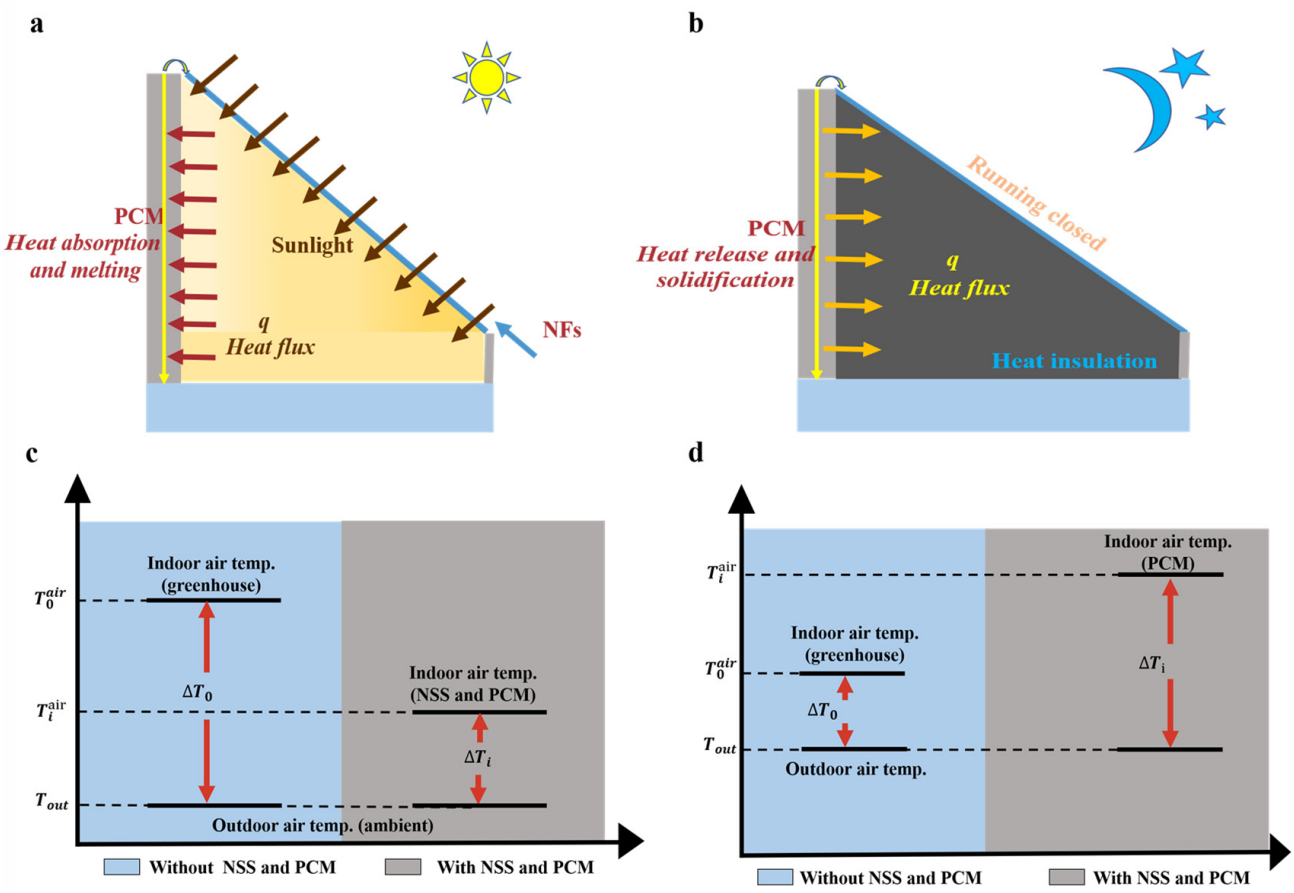


**Figure 2.** The thermal model of the NSS-PCM system during daytime (**a**) and nighttime (**b**), the temperature difference during the daytime (**c**), and the increase in temperature difference during nighttime (**d**).

## 3. Experiment and Model

### *3.1. Experimental Testing on Thermal Environment*

The experiment (Figure 3) was carried out over 75 days, from 28 February to 16 May 2024, in Nanjing (32.06° N, 118.78° E). During the initial 15 days, this experiment mainly tested the thermal performance and sunlight wavelength distribution in the greenhouse roof. In this experiment, a small greenhouse (1.2 × 0.5 × 1.5 m) was built. The roof greenhouse was a south-oriented roof at a 45° angle and 0.72 $m^2$ area (1.2 × 0.6 m) based on the article by Yuan [16]. The greenhouse roof was covered by the NSS receiver. The NSS was composed of acrylic glass plates (PMMA) with a thickness of 10 mm and nanofluids flowing inside at the rate of 7 L/min. The aluminum trough (0.5 × 0.02 × 1 m) was arranged on the back of the greenhouse and was filled with PCMs. The vertical copper tubes were placed in the PCMs. The other four sides of the greenhouse were composed of aluminum plates with a 15 cm thick thermal insulation layer. The CNT nanofluids with a concentration of $1 \times 10^{-6}$ kg/$m^3$ were used. The organic paraffin wax was used as the PCM. The type of paraffin was ZJ-PCM-A-18. The phase transition temperature was 18 °C, and the latent enthalpy was 200 J/g. The total length of the serpentine copper tube used was about 10 m, and the diameter was 0.01 mm.

In the 75 days, this experiment mainly monitored the growth of vegetables in the greenhouse and the content of nutrients after maturity. After about 75 days of growth, three vegetables were harvested by cutting branches on the surface of the soil and carefully separating the roots from the sandy substrate [39]. The branches and roots were washed with distilled water, dried with tissue paper, and weighed. The shoots and roots were

then separated, and the height and leaf count of each plant were recorded. Afterward, the samples were dried at 75 °C for 48 h to assess dry weight and micronutrient concentration. Moisture content (MC) was determined through direct drying in a drying oven and expressed as a percentage. The sample was measured three times, and the average value was taken [40]. The plants were divided into roots, stems, and leaves, and their fresh weights were recorded individually. The dry matter content for the roots, stems, and leaves was calculated as follows:

$$\text{Dry matter content (\%)} = \text{dry matter weight/fresh matter weight} \times 100\% \quad (1)$$

The spectral illuminometer was used to measure the light band and intensity entering the greenhouse. Agilent was used to measure the temperature of each area of the greenhouse. The irradiator was used to measure the solar radiation intensity. The model and accuracy of the experimental instruments are shown in Table 1.

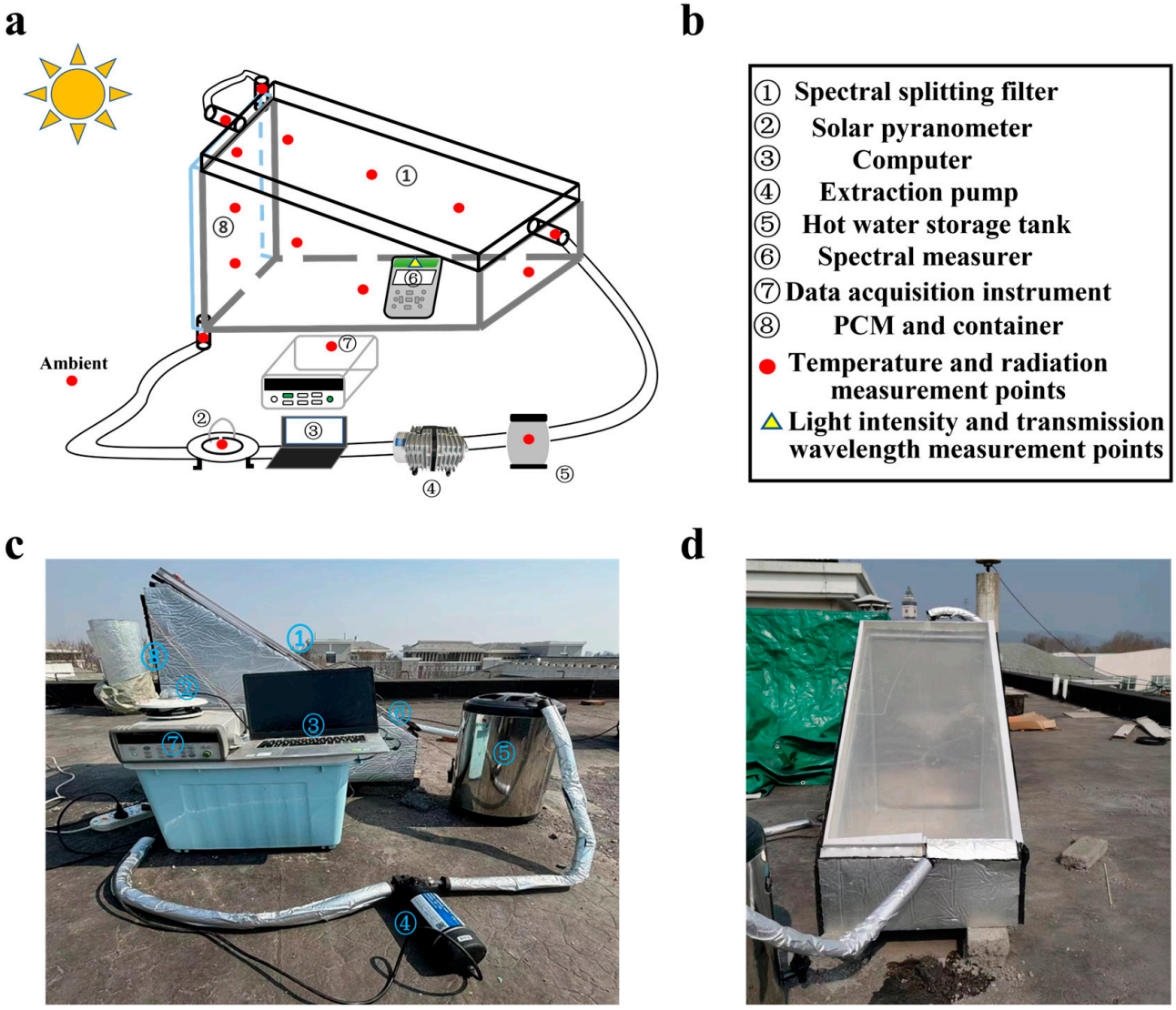


**Figure 3.** The model (**a**), the digital representation (**b**) and the side (**c**) and front (**d**) of the solar greenhouse with NSS-PCMs.

**Table 1.** Experimental instruments.

| Apparatus | Model | Measuring Parameter | Accuracy |
|---|---|---|---|
| Data acquisition instrument | Agilent34972 A | Temperature, solar radiation intensity | / |
| Thermocouple | K type | Temperature | ±0.5 °C |
| Extraction pump | T43-220 | / | ±0.5% |
| Spectral illuminometer | HPCS-3200 | Wavelength transmittance | / |
| Solar irradiator | TQB-2 | Global solar radiation | ±11.04 |
| Hot-wire anemometer | KANOMAX | Airflow velocity | ±5% or ±0.015 m/s |

### *3.2. Thermal Model System*

In this study, the simulation process was conducted using MATLAB-R2023b software. We developed a mathematical model based on heat transfer and energy balance in MATLAB to simulate temperature distribution and thermal efficiency within the greenhouse (Figure 4). The model incorporates heat sources, heat losses, the heat storage and release mechanism of phase change materials, as well as external environmental conditions (such as solar radiation and air temperature). By discretizing the model and performing time-stepping simulations, we analyzed temperature variations under different conditions and validated the model with experimental data to ensure its accuracy.

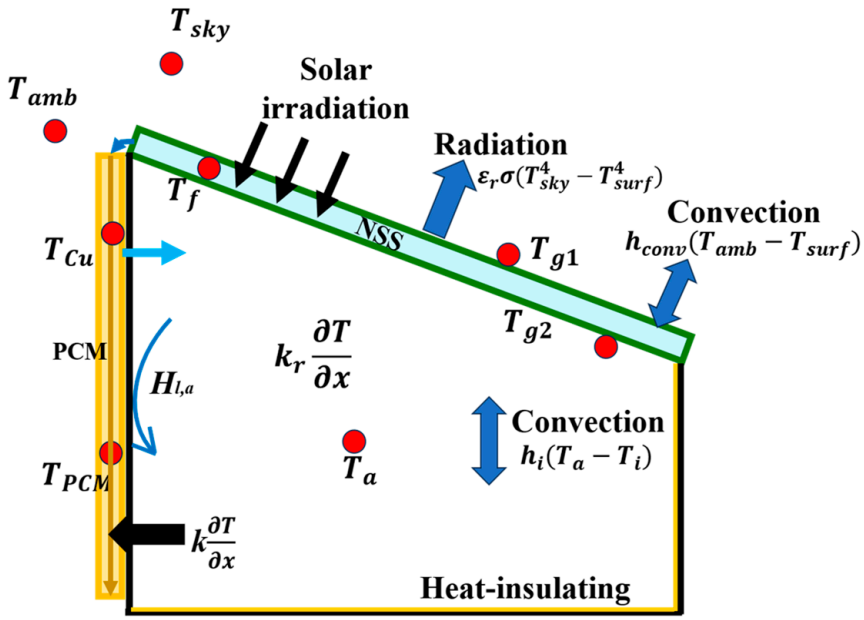


**Figure 4.** Model for the thermal model system.

In the numerical model, $T_{g1}$, $T_{g2}$, $T_a$, $T_f$, $T_l$, $T_{Cu}$, $T_i$, and $T_{PCM}$ (°C) are the temperatures of the glass cover, the bottom surface of the glass plate, greenhouse air, nanofluids, the PCM container aluminum, serpentine copper tubes, and the inside temperature of each wall and PCMs, respectively.

The energy balance equation for the greenhouse glass panel is given by

$$\rho_{g1}\delta_{g1}c_{g1}\frac{\partial T_{g1}}{\partial t} = G_{g1} + h_{c\_abm}\left(T_{amb} - T_{g1}\right) + h_{r\_sky}\left(T_{sky} - T_{g1}\right) + h_{c\_g1f}\left(T_f - T_{g1}\right) + h_{r\_g1f}\left(T_f - T_{g1}\right) \quad (2)$$

where $\rho_{g1}$ (kg·m$^{-3}$) is the density of glass cover; $\delta_{g1}$ (m) is the thickness of the upper glass panel; $c_{g1}$ (J·K$^{-1}$·m$^{-2}$) is the capacity of the glass panel; $G_{g1}$ (W·m$^{-2}$) is the solar radiation

intensity on the upper surface of the glass plate; $h_{c\_abm}$ ($W \cdot m^{-2} \cdot K^{-1}$) is the convective heat transfer coefficient between glass and ambient air; $h_{r\_sky}$ ($W \cdot m^{-2} \cdot K^{-1}$) is the sky temperature radiation coefficient; and $h_{c\_g1f}$ and $h_{r\_g1f}$ ($W \cdot m^{-2} \cdot K^{-1}$) are the convective heat transfer coefficient and the radiant heat transfer coefficient between the upper glass panel and nanofluids, respectively.

The energy balance equation for the solar radiation intensity of the model is given by

$$G_{g1} = \int_{300}^{4000} \alpha_g(\lambda) G(\lambda) d\lambda sin(h) cos(\beta) \tag{3}$$

$$sin(h) = sin\phi sin\delta + cos\phi cos\delta cosh_a \tag{4}$$

where $\varphi$ is the dimension of the location; $\delta$ is the solar declination; $h_a$ is the solar hour angle; and $\beta$ is the tilt angle.

$$h_{r\_sky} = \sigma \varepsilon_g \left(T_{sky} + T_{g1}\right)\left(T_{sky}^2 + T_{g1}^2\right) \tag{5}$$

$$h_{r\_g1f} = \frac{\sigma\left(T_{g1} + T_f\right)\left(T_{g1}^2 + T_f^2\right)}{1/\varepsilon_g + 1/\varepsilon_f} \tag{6}$$

The energy balance equation for sky temperature [41] is given by

$$T_{sky} = 0.0552 T_a^{1.15} \tag{7}$$

$$h_{c\_abm} = 6.5 + 3.3 u_a \tag{8}$$

The Nusselt number in the greenhouse is given as [42]

$$Nu_f = 0.664 Re_g^{1/2} Pr_g^{1/3} \tag{9}$$

$$h_{c\_g1f} = \frac{Nu_f \lambda}{l_g} \tag{10}$$

The energy balance equation for bottom surface of the glass plate in the greenhouse is given as

$$\begin{aligned} \rho_{g2} \delta_{g2} c_{g2} \frac{\partial T_{g2}}{\partial t} &= G_{g2} + h_{c\_g2f}\left(T_f - T_{g2}\right) + h_{c\_ag2}\left(T_a - T_{g2}\right) + h_{r\_lg2}\left(T_l - T_{g2}\right) \\ &+ h_{r\_fg2}\left(T_f - T_{g2}\right) \end{aligned} \tag{11}$$

where $h_{r\_g2f}$ and $h_{c\_g2f}$ ($W \cdot m^{-2} \cdot K^{-1}$) are the radiation heat transfer coefficient and convective heat transfer coefficient between the lower glass panel and nanofluids, respectively.

$$G_{g2} = \int_{300}^{800} \tau_g(\lambda) \tau_f(\lambda) \alpha_g(\lambda) G(\lambda) d\lambda sin(h) cos(\beta) \tag{12}$$

$$h_{r\_g2f} = \frac{\sigma\left(T_{g2} + T_f\right)\left(T_{g2}^2 + T_f^2\right)}{1/\varepsilon_g + 1/\varepsilon_f} \tag{13}$$

The energy balance equation for the air inside the roof greenhouse sky temperature is given by

$$\begin{aligned} \rho_a \delta_a c_a \frac{\partial T_a}{\partial t} &= h_{c\_ag2}\left(T_{g2} - T_a\right) + h_{r\_ag2}\left(T_{g2} - T_a\right) + h_{r\_al}\left(T_l - T_a\right) \\ &+ h_{c\_al}\left(T_l - T_a\right) + \sum h_{c,i}\left(T_i - T_a\right) \end{aligned} \tag{14}$$

where $h_{c\_ag2}$ and $h_{r\_ag2}$ ($W \cdot m^{-2} \cdot K^{-1}$) are the convective heat transfer coefficient and radiation heat transfer coefficient between the lower glass panel and greenhouse air, respectively; $h_{r\_al}$ and $h_{c\_al}$ ($W \cdot m^{-2} \cdot K^{-1}$) are the radiation heat transfer coefficient and convective heat transfer coefficient between greenhouse air and PCM container, respectively; and $h_{c,i}$ ($W \cdot m^{-2} \cdot K^{-1}$) is the heat transfer coefficient between each wall surface and room air.

$$h_{c,i} = 2.03\Delta T^{0.14} \tag{15}$$

$$h_{r\_al} = \frac{\sigma(T_a + T_l)\left(T_a^2 + T_l^2\right)}{1/\varepsilon_a + 1/\varepsilon_l} \tag{16}$$

The energy balance equation for the nanofluids in the NSS receiver in the roof greenhouse is given by [43]

$$\begin{aligned} \rho_f \delta_f c_f \frac{\partial T_f}{\partial t} &= G_f + h_{c\_g1f}\left(T_{g1} - T_f\right) + h_{c\_g2f}\left(T_{g2} - T_f\right) + h_{r\_g1f}\left(T_{g1} - T_f\right) \\ &+ h_{r\_g2f}\left(T_{g2} - T_f\right) - \rho_f \nu \delta_f c_f \frac{\partial T_f}{\partial x} \end{aligned} \tag{17}$$

$$G_f = \int_{800}^{4000} \tau_g(\lambda)\alpha_f(\lambda)G(\lambda)d\lambda sin(h)cos(\beta) \tag{18}$$

The energy balance equation for the inner wall of the PCM container aluminum in the greenhouse is given as

$$\rho_l \delta_l c_l \frac{\partial T_l}{\partial t} = G_l + h_{r\_lg2}(T_{g2} - T_l) + \frac{k_l}{\delta_l}(T_{pcm} - T_l) + h_{c\_al}(T_a - T_l) + h_{r\_al}(T_a - T_l) \tag{19}$$

where $k_l$ ($W \cdot m^{-2} \cdot K^{-1}$) is the thermal conductivity of aluminum plate, and $h_{r\_lg2}$ ($W \cdot m^{-2} \cdot K^{-1}$) is the radiation heat transfer coefficient of the lower glass and the PCM container.

$$G_l = \int_{300}^{800} \tau_g^2(\lambda)\tau_f(\lambda)\alpha_l(\lambda)G(\lambda)sin(h)cos(\beta)d\lambda \tag{20}$$

$$h_{r\_lg2} = \frac{\sigma\left(T_{g2} + T_l\right)\left(T_{g2}^2 + T_l^2\right)}{1/\varepsilon_g + 1/\varepsilon_l} \tag{21}$$

The energy balance equation for the snake-shaped copper tube in the greenhouse is given as

$$\rho_{Cu}\delta_{Cu}c_{Cu}\frac{\partial T_{Cu}}{\partial t} = h_{c\_fCu}\left(T_f - T_{Cu}\right) + \frac{k_{Cu}}{\delta_{Cu}}(T_{pcm} - T_{Cu}) - \rho_f \nu \delta_f c_f \frac{\partial T_{nf}}{\partial x} \tag{22}$$

where $k_{Cu}$ ($W \cdot m^{-2} \cdot K^{-1}$) is the thermal conductivity of copper tube, and $h_{c\_fCu}$ and $h_{r\_Cuf}$ ($W \cdot m^{-2} \cdot K^{-1}$) are the convective heat transfer coefficient and radiative heat transfer coefficient between nanofluids and copper tube, respectively.

$$h_{c\_fCu} = \frac{Nu_{Cu}\lambda}{l_{Cu}} \tag{23}$$

$$Nu_{Cu} = 0.664 Re_{Cu}^{1/2} Pr_{Cu}^{1/3} \tag{24}$$

The energy balance equation for nanofluids in the snake-shaped copper tube is given as [44]

$$\rho_f \delta_f c_f \frac{\partial T_{nf}}{\partial t} = h_{c\_fCu}\left(T_{Cu} - T_f\right) + h_{r\_Cuf}\left(T_{Cu} - T_{nf}\right) \tag{25}$$

$$h_{r\_Cuf} = \frac{\sigma\left(T_{Cu} + T_f\right)\left(T_{Cu}^2 + T_f^2\right)}{1/\varepsilon_f + 1/\varepsilon_{Cu}} \tag{26}$$

The energy balance equation for the PCMs in the roof greenhouse is given by [45,46]

$$\rho_{PCM} c_{PCM} \frac{\partial T_{PCM}}{\partial t} = \frac{\partial}{\partial x}\left(k_{PCM} \frac{\partial T_{PCM}}{\partial x}\right) + Q_{latent} + h_{c\_Cu}(T_{Cu} - T_{PCM}) + h_{c\_l}(T_l - T_{PCM}) \tag{27}$$

where $\boldsymbol{Q_{latent}}$ (J) is the latent heat of the PCMs, and $\boldsymbol{h_{c\_Cu}}$ and $\boldsymbol{h_{c\_l}}$ ($W \cdot m^{-2} \cdot K^{-1}$) are the convective exchange coefficients between the copper tube and PCMs and between the aluminum plate and PCMs, respectively.

$$Q_{latent} = \rho_{PCM} H\left(\frac{\partial \Phi}{\partial t} + \frac{\partial \Phi_{solid}}{\partial t}\right) \tag{28}$$

$T_{PCM}$ is the internal temperature of the phase change material. The calculation formula is as follows [45]:

$$T_{pcm} = \begin{cases} H_p / c_{PCM} + T_m & H_p \le H_s \\ \left(H_p - L\right) / c_{PCM} + T_m & H_p \ge H_l \\ T_m & H_s < H_p < H_l \end{cases} \tag{29}$$

$$H_s - H_l = H \tag{30}$$

where $\boldsymbol{T_m}$ (K) is the transformation temperature of the PCMs.

After establishing the heat transfer model, the energy conservation equations for each part were discretized. The measured indoor and outdoor meteorological parameters, including solar radiation intensity, outdoor air temperature, outdoor air velocity, and indoor air temperature, were used as boundary conditions. These parameters were compiled into a MATLAB code file and imported for calculation. The initial temperature values were based on pre-experiment measurements, and the temperature of each part was calculated sequentially. All physical parameters used are shown in Table 2.

**Table 2.** The physical parameters.

| Material | Acrylic Glass | NF | PCM | Copper Tube | Aluminum | Air | Heat Insulation Layer |
|---|---|---|---|---|---|---|---|
| $\alpha$ | | 0.1 | | 0.05 | 0.2 | 0.2 | |
| $\varepsilon$ | | | | 0.02 | 0.06 | | |
| $c_p$, J/kg·K | 1900 | 4180 | 2500 | 390 | 903 | 1005 | 330 |
| Thickness, m | 0.01 | 0.01 | 0.02 | 0.05 | 0.001 | | 0.015 |
| $\rho$, kg/m$^3$ | 1200 | 1000 | 880 | 8960 | 2702 | 1.16 | 30 |
| $\lambda$, W/m$^2$·K | 0.22 | 0.7 | 0.4 | 398 | 237 | 0.026 | 0.035 |
| Transmittance | 0.93 | 0.9 | | | | 1 | |

Figure 5 shows the flow diagram of the calculation process. In this process, the equations for each node were numerically discretized using the implicit method, with a time step of 1 s. The input data includes initial conditions, boundary conditions, and physical parameters, which are used to initialize the calculations. As each time step progresses, the implicit method solves the equations for each node and updates the corresponding variable values (temperature, pressure, or velocity). After each time step, the output results display the calculated state of each node, including the values of physical quantities, which are then used to analyze the system's dynamic behavior and verify optimization results.

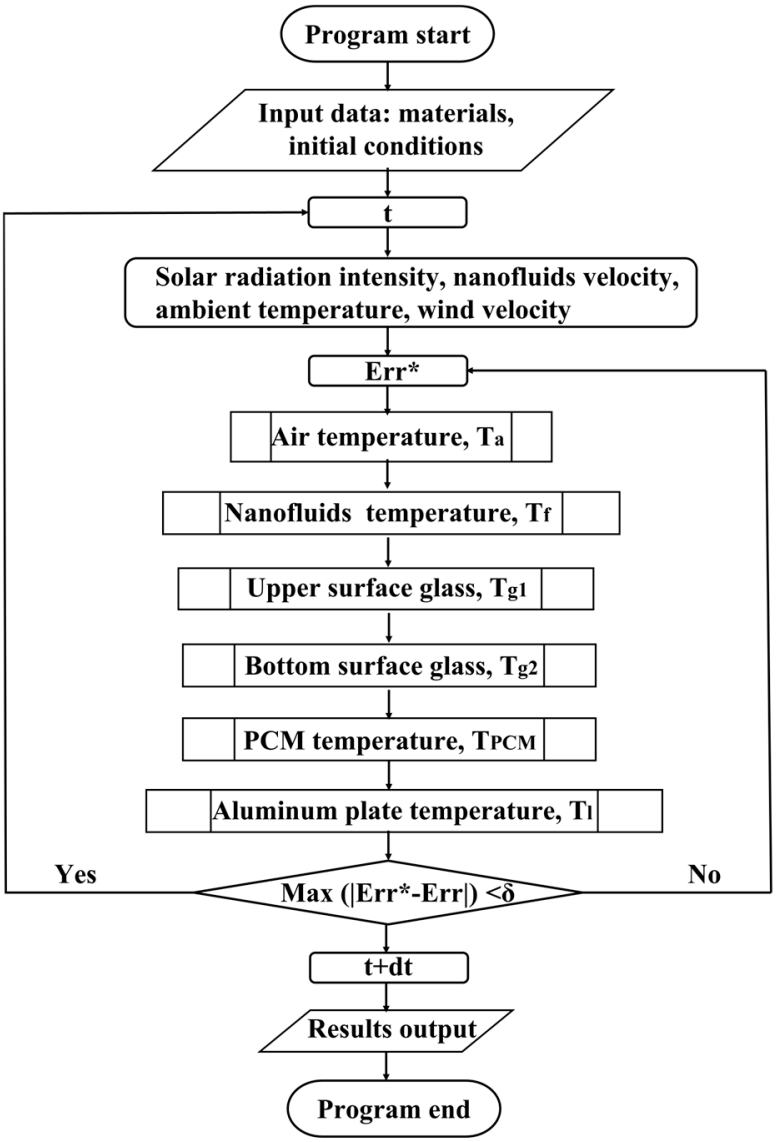


**Figure 5.** The calculation process for the thermal model system.

### *3.3. Performance Evaluation*

The measured photothermal conversion efficiency ($\eta_{th}$) of the solar greenhouse with the NSS-PCM system can be calculated based on Equation (31) [47].

$$\eta_{th} = \frac{c_{P,NF}\rho_{NF}V_{flow}(T_{outlet} - T_{inlet}) + Q}{E_{Sun}A_{NSS}} \tag{31}$$

where $A_{NSS}$ ($m^2$) is the area of the NSS-PCMs; $E_{Sun}$ is the sunlight incident on the NSS surface; $V_{flow}$ ($L \cdot h^{-1}$) is the flow rate; $T_{inlet}$ and $T_{outlet}$ (°C) are the inlet and outlet temperatures of the nanofluids, respectively; $c_{p,NF}$ ($J \cdot kg^{-1} \cdot K^{-1}$) is the specific heat capacity of the nanofluids; $\rho_{NF}$ ($kg \cdot m^{-3}$) is the density of the nanofluids; $V_{flow}$ ($L \cdot h^{-1}$) is the flow rate; and $Q$ is the heat obtained by heat conduction.

The energy balance equation for thermal efficiency ($\eta$) is given by

$$\eta = \frac{Q_f + Q + G_a A}{E_{sun}A_{NSS}} \tag{32}$$

where $Q_f$ is the heat obtained by thermal convection, and $G_a$ is the heat obtained by radiative heat transfer.

The calculation formula of PCM is shown below [48]:

$$Q = Q_S + Q_L \tag{33}$$

$$Q_s = \int_0^{T_c} c_p m dT + \int_{T_c}^{T} c_p m dT \tag{34}$$

$$Q_L = c_p m T_C \tag{35}$$

where $\boldsymbol{Q_s}$ is the apparent heat of phase transition (J); $\boldsymbol{Q_L}$ is the latent heat of phase change (J); $\boldsymbol{c_p}$ is the specific heat capacity of the PCMs (J/kg·K); and $\boldsymbol{T_c}$ is the phase change temperature (°C).

The greenhouse room can be treated as a whole system, and the room exchanges heat with the surroundings mainly through heat conduction during nighttime. The calculation formula for heat loss of the room is shown below [49]:

$$Q_l = \frac{(T - T_{abm})\lambda}{L/S} \tag{36}$$

where $\boldsymbol{\lambda}$ is the thermal conductivity (W/m·k); $\boldsymbol{L}$ is the thickness of the object (m); $\boldsymbol{T}$ is the temperature of the object; and $\boldsymbol{T_{abm}}$ is the ambient temperature around the object.

## 4. Results and Discussion

### *4.1. System Structure Optimization*

#### 4.1.1. One-Day Thermal Environment and Model Verification

Before formal vegetable planting, a one-day thermal environment experiment was conducted, and the results were analyzed, modeled, and optimized. Solar irradiation varied from 0 to 625.85 W/m$^2$, averaging 467.75 W/m$^2$ during the day. The outdoor temperature around the greenhouse ranged from 15 to 20 °C in the daytime and 7 to 9 °C at night, with wind speeds of 1–3 m/s (Figure 6a). As solar radiation increased, the indoor temperature rose, peaking around 2:00 p.m., then gradually dropped as radiation decreased. The temperature fluctuated between 10 and 20 °C from 8:00 p.m. to 8:00 a.m. due to the release of heat from phase change materials, which helped maintain indoor temperature stability (Figure 6b). During the daytime, the greenhouse temperature was higher than outside because the highly transparent acrylic glass allowed solar radiation to enter directly. The enclosed space trapped heat, and the ground and walls absorbed solar energy, transferring it to the indoor air. The temperature inside the greenhouse was 5–6 °C higher than the outside ambient temperature during nighttime, as PCMs absorbed heat from nanofluids during daytime and gradually released it during nighttime, keeping the indoor environment warmer.

The phase transition began around 10:00 a.m. and lasted about 4 h. Heat release from the phase change started at 7:00 p.m. and continued for approximately 6 h (Figure 6c). The difference between the absorption and release time was due to the radiation heat absorbed by the aluminum plate, which transferred the heat to the PCMs during daytime. However, the PCMs did not achieve the expected continuous heat release. This was partly because the nanofluid flow was insufficient, limiting the heat absorbed by the PCMs, and partly because the PCM layer was too thin to fully utilize the nanofluid's heat. Therefore, we further optimized the hybrid system, which will be discussed in Section 4.2. The thermal efficiency of the experimental system was more than 20% (Figure 6d), which had a good effect compared with the article by Yuan [16]. As the temperature gradient between the greenhouse and the outdoor environment increased, the solar greenhouse with the NSS-PCM system experienced greater heat loss. The efficiency ($\boldsymbol{\eta th}$) decreased between 10:00 a.m. and 04:00 p.m. because the roof greenhouse functions as a closed system. As

irradiation intensity rose, more heat was absorbed, resulting in an increased temperature gradient between the interior and exterior environments. However, from 3:30 p.m. to 5:30 p.m., the efficiency began to increase as the irradiation intensity decreased and the PCMs released stored heat, maintaining a stable temperature gradient between the roof greenhouse and the outside ambient temperature (Figure 6d).

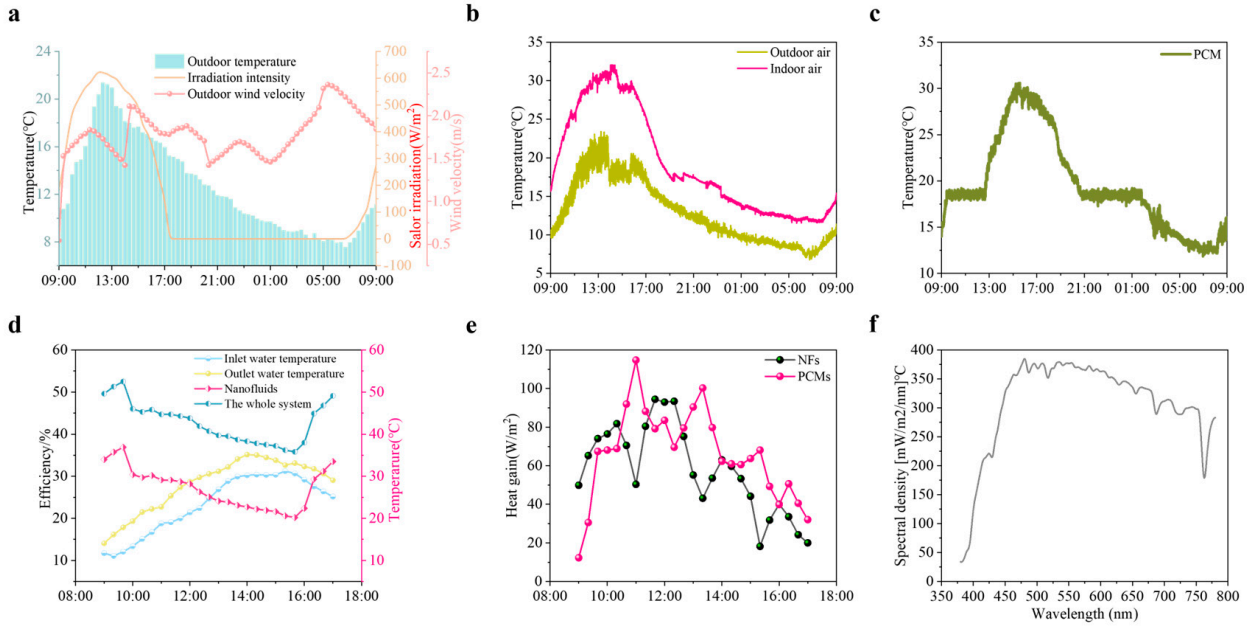


**Figure 6.** The weather parameters (**a**), comparison of greenhouse indoor air and outside ambient temperature (**b**), the temperature of PCMs (**c**), the photothermal conversion efficiency and thermal efficiency (**d**), the heat gain of nanofluids and PCMs during daytime (**e**), and the light intensity distribution inside the greenhouse (**f**).

As the heat absorption of the PCM increased, the heat absorption of the nanofluid decreased, as the heat absorbed by the PCM from the nanofluid and solar radiation was continuously fluctuating. The peak wavelength was 480.6 nm, and the light in the 300–800 nm range, crucial for plant growth, had high transmittance. Typically, plants need light energy density between 100 and 1000 mW/m$^2$/nm for photosynthesis (Figure 6f). The average light intensity of all the day fell in this range. From 09:00 a.m. to 01:30 p.m., the transmittance of 300–800 nm light increased with rising solar radiation, but from 1:30 p.m. to 5:00 p.m., it decreased as a result of reduced solar radiation and the shifting angle of the sun. Notably, the NSS receiver maintained over 80% transmittance in the 300–800 nm range, optimal for plant growth (Figure 7).

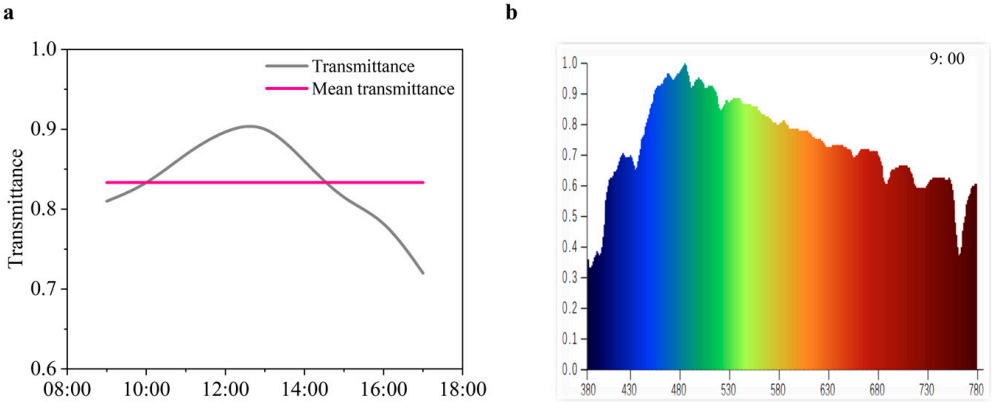


**Figure 7.** *Cont.*

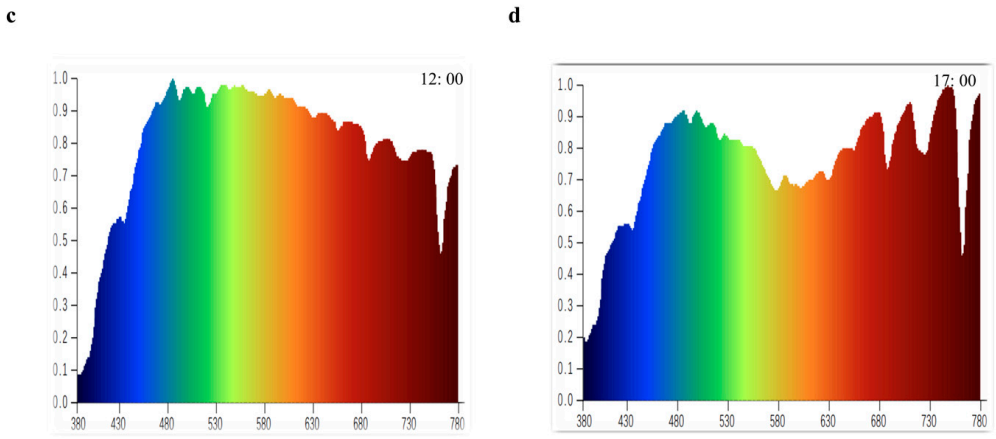


**Figure 7.** The average transmittance of light (**a**) and transmittance at 9:00 (**b**), 12:00 (**c**), and 17:00 (**d**).

#### 4.1.2. Parameter Optimization

The experimental values closely matched the simulated values presented in Figure 8, demonstrating a strong correlation between the two sets of data. However, slight discrepancies were noted. These differences can be attributed to the experimental data being collected with Agilent equipment, which recorded significant temperature fluctuations during the experiments. Previous studies have indicated that during nighttime, the indoor temperature often drops below 15 °C, leading to a halt in the heat release from the phase change materials (PCMs). Additionally, the temperature of the nanofluids remained relatively high, suggesting that a portion of the absorbed heat was not fully utilized for plant growth or other heating needs.

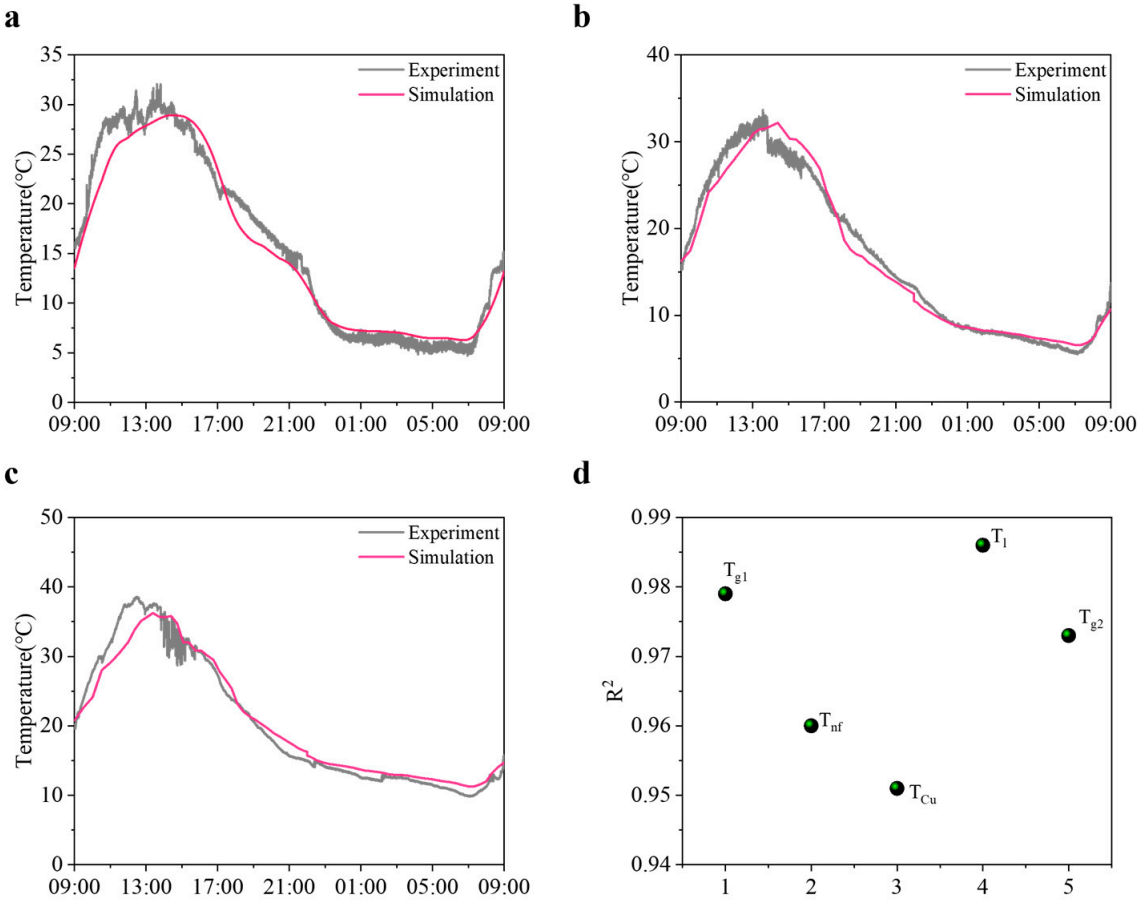


**Figure 8.** The temperature of the glass cover (**a**), glass plate (**b**), aluminum plate on the inner wall of the PCM container (**c**), and the $R^2$ of other parts (**d**).

To address these challenges and enhance the efficiency of the system, further refinements were made by simulating variations in the thickness of the phase change layer and adjusting the phase transition temperature of the PCMs. These modifications aimed to optimize heat retention and improve overall energy management within the greenhouse environment, thereby ensuring that both the nanofluids and PCMs can operate more effectively in providing the necessary thermal conditions for optimal plant growth.

To further enhance the performance of the system, we optimized the phase change thickness to 2 cm, 3 cm, and 4 cm. The results indicated that from 9:00 a.m. to 3:00 p.m., indoor air temperatures decreased as the phase change thickness increased (Figure 9a). This was because thicker phase change materials could effectively improve heat absorption, thereby lowering the temperature and thermal radiation of the nanofluids. Conversely, from 3:00 p.m. to 9:00 a.m. the next day, indoor temperatures increased with higher phase change thickness due to increased heat storage and prolonged heat release (Figure 9a). When the phase change thickness reached 4 cm, the indoor temperature remained at 15–18 °C for most of the night, providing a stable environment for plant growth. As the phase change thickness increased, the peak temperature gradually decreased and occurred later (Figure 9b). This was due to the need for thicker phase change materials to absorb more heat, leading to longer phase transition times. During the exothermic phase, thicker phase change materials could store more heat, resulting in higher indoor temperatures. Additionally, the photothermal conversion efficiency increased with greater phase change thickness, as thicker materials could more effectively absorb and store solar radiation.

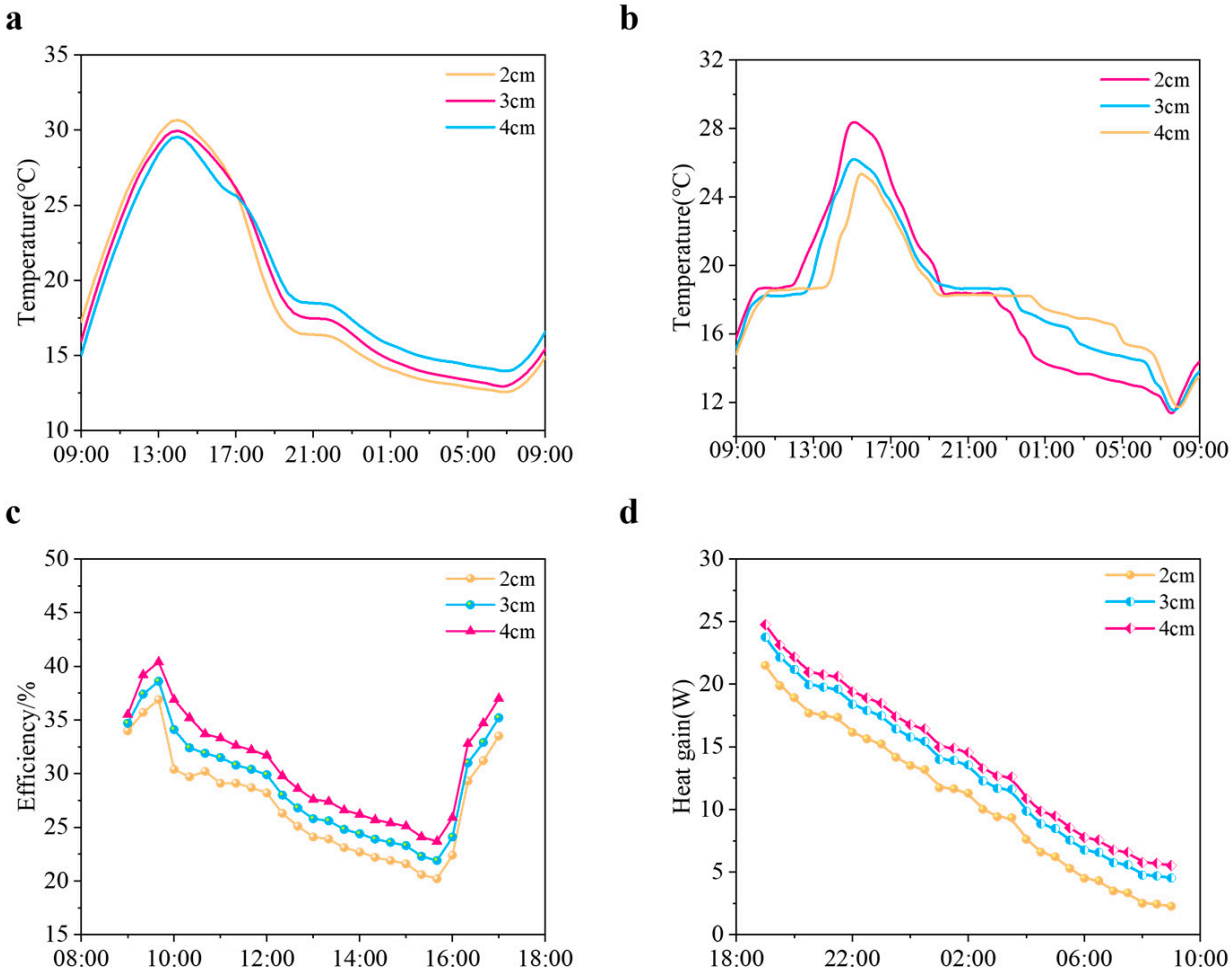


**Figure 9.** Comparison of indoor air temperature (**a**), PCM temperature (**b**), thermal efficiency (**c**), and heat gain (**d**) of three different PCM layer thicknesses after optimization.

The thermal efficiency of the system exhibited a pattern of initially rising, then decreasing, and finally increasing again (Figure 9c). In the early stages, the solar radiation intensity was low, resulting in slow heat accumulation and a gradual rise in thermal efficiency. At noon, as solar radiation intensity increased, heat storage peaked, causing a corresponding increase in thermal efficiency. However, as solar radiation gradually diminished and nighttime approached, thermal efficiency began to decline, primarily due to increased heat loss and lower ambient temperatures. Notably, during the night, especially with a phase change thickness of 4 cm, the system was still able to maintain a relatively stable indoor temperature. This indicates that the optimized phase change thickness not only improved the thermal efficiency of the system but also effectively extended heat release time, providing more suitable conditions for plant growth. These findings offer important theoretical support and practical guidance for the future design of rooftop greenhouses and the application of phase change materials.

Furthermore, we optimized the phase transition temperature. In the simulation, the initial indoor air temperature decreased with the increase in the phase transition temperature (Figure 10a). This was because the higher phase transition temperature improved the absorption of heat, resulting in a decrease in the temperature and thermal radiation of the nanofluid. However, from 03:00 p.m. to 09:00 a.m. the next day, as the phase transition temperature rose, the indoor temperature began to pick up, mainly due to increased heat storage and longer heat release times. When the phase transition temperature was set to 22 °C, the indoor temperature was maintained at 15–18 °C on most nights. With the increase of phase transition temperature, the peak value of indoor temperature gradually decreased, and the occurrence time was delayed accordingly (Figure 10b). This caused the time required for the phase transition to become longer because more heat needed to be absorbed. In the exothermic stage, the higher phase transition temperature allowed more heat to be stored, resulting in an increase in indoor temperature.

The thermal efficiency of the system showed a dynamic change pattern (Figure 10c), initially rising, then falling, and finally rising again. This fluctuation reflected the influence of changes in solar radiation intensity and heat loss during the day. In the morning, low-intensity solar radiation caused heat loss, resulting in a decrease in thermal efficiency, while at noon, the enhanced solar radiation promoted the absorption of heat and increased the thermal efficiency. However, as the afternoon progressed, solar radiation weakened and heat losses increased, again affecting thermal efficiency. Overall, these findings highlight the importance of phase transition temperature in regulating indoor climate stability and optimizing the thermal performance of solar greenhouse systems. By optimizing the phase transition temperature, we can more effectively manage the thermal environment in the greenhouse and improve conditions for crop growth.

The solar greenhouse equipped with the NSS-PCM system demonstrated exceptional advantages in temperature regulation, especially in environments with intense sunlight and significant temperature differences between day and night. The results showed that during the peak temperature period from 11:00 a.m. to 05:00 p.m., this system effectively lowered the internal temperature of the greenhouse. This cooling effect is attributed to the high absorption spectrum (HAS) characteristics of the nanofluids, which absorb solar radiation energy and store it as thermal energy, thereby preventing excessive heat accumulation within the greenhouse. The average internal temperature of greenhouses equipped with the NSS-PCM system was 3–4 °C lower than that of those without the system (Figure 10d). This significant cooling effect not only protects plants from high temperatures but also helps reduce transpiration rates, optimizing water resource management. During intense sunlight, the cooling effect of this system will be particularly pronounced. Strong solar radiation can cause the internal temperature of conventional greenhouses to rise sharply,

posing a risk of heat stress to crops. High-temperature environments can lead to a decrease in photosynthetic efficiency, cell damage, and even metabolic imbalances in plants. By employing an active temperature management approach that absorbs heat and lowers temperatures, the NSS-PCM system mitigates the excessive heat accumulation inside the greenhouse. Consequently, plants can grow under more suitable temperature conditions, reducing growth fluctuations during high-temperature periods and ensuring stable growth rates and yields.

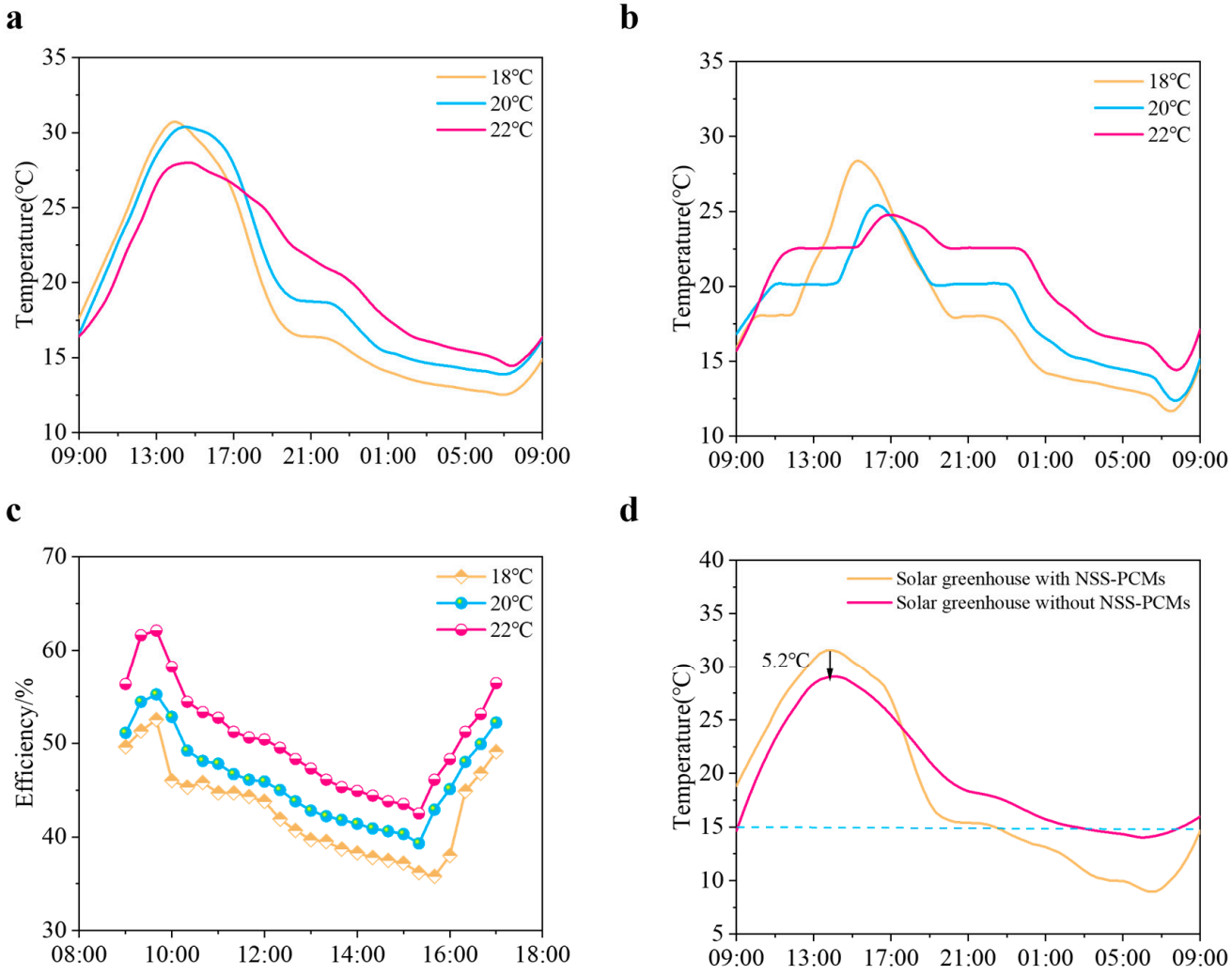


**Figure 10.** Comparison of indoor air (**a**) and PCM temperature (**b**) after optimization and thermal efficiency (**c**) of the system of three different phase transition temperatures and comparison of indoor air in two solar greenhouse systems (**d**).

During nighttime, the NSS-PCM system demonstrated excellent temperature control by releasing the heat absorbed during the day, thus providing a warming effect. The results showed that between 06:00 p.m. and 09:00 a.m. the following morning, the internal temperature of greenhouses equipped with this system was 5–6 °C higher than that of those without it (Figure 10d). This nighttime warming mechanism effectively protects crops from low temperatures, preventing growth inhibition due to cold conditions. Particularly in winter or in regions with significant temperature drops at night, a sudden decrease in temperature can lead to freezing or stunted growth in plants and, in severe cases, can result in plant death. The NSS-PCM system provides crucial heat supply during these times by releasing the stored thermal energy in the phase change materials, helping to maintain a

relatively constant temperature within the greenhouse, ensuring that crops can continue their physiological activities even during cold nights and early mornings.

Moreover, this nighttime warming effect positively impacts the photosynthesis and metabolic processes of plants. Temperature is a key factor influencing plant metabolism, and low temperatures can lead to reduced metabolic rates, affecting nutrient absorption and assimilation processes. By maintaining suitable temperatures during the night, the NSS-PCM system ensures that plant metabolism remains stable, allowing crops to maintain a certain growth rate even at night, thereby enhancing overall growth efficiency.

### *4.2. 75-Day Thermal Environmental Tests in Greenhouse*

Based on the optimized model, a comprehensive 75-day thermal environment test of the novel greenhouse was conducted, recording temperature variations both inside and outside from 29 February to 15 May (Figure 11). The results indicated that during the daytime, the indoor temperature of the greenhouse consistently remained approximately 10 °C higher than the outdoor temperature. This significant temperature difference is attributable to the roof greenhouse's effective heat-collecting properties and its enclosed design, which capture and store solar energy efficiently. At night, the indoor temperature stabilized around 15 °C (Figure 11b), thanks in large part to the strategic use of phase change materials (PCMs). These materials play a crucial role in regulating the greenhouse environment. During the day, the PCMs absorb excess heat, preventing overheating that can stress the plants. When nighttime arrives and temperatures drop, the PCMs release the stored heat, mitigating excessive cooling and ensuring a stable temperature. This process maintains an optimal environment conducive to plant growth, supporting critical physiological and metabolic processes essential for healthy development.

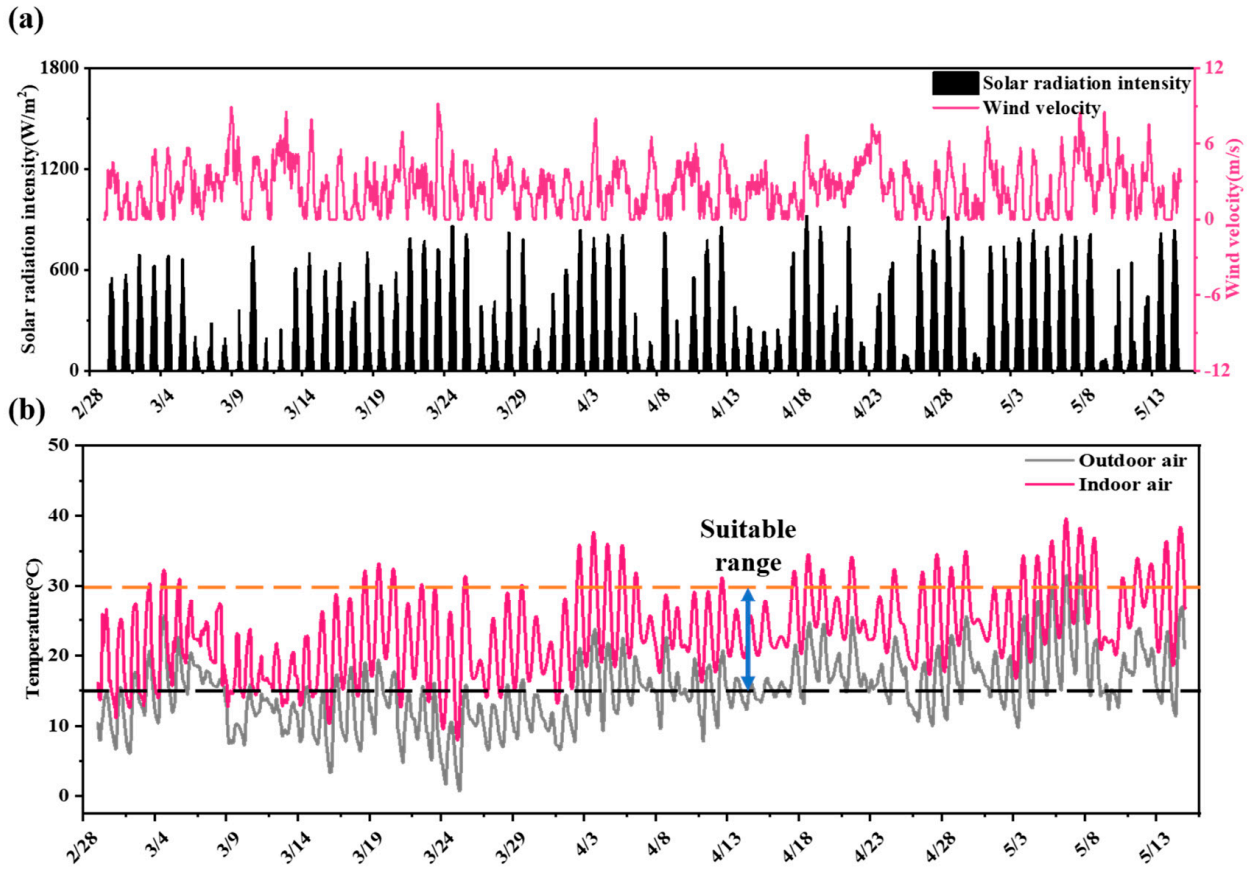


**Figure 11.** The outdoor parameters (**a**) and comparison of indoor and outdoor air temperature of the novel greenhouse (**b**).

Furthermore, the integration of nanofluids into the lighting system significantly enhances photosynthetic efficiency. Nanofluids possess unique spectroscopic properties that not only prevent temperature spikes within the greenhouse but also provide an optimal light spectrum (300–800 nm) essential for photosynthesis. This capability ensures even light distribution across the plants, guaranteeing sufficient light exposure. As a result, plants are better able to carry out photosynthesis effectively, leading to increased accumulation of organic matter and overall growth. This dual approach of using phase change materials for temperature regulation and nanofluids for optimized light conditions illustrates the innovative design of the greenhouse, aimed at maximizing plant health and productivity in a controlled environment.

To further clarify the experimental results, we carefully selected 4 to 5 days of data from each month for detailed analysis (Figure 12a–d). This specific data allowed for a comprehensive assessment of the performance and stability of the greenhouse system, thereby more accurately verifying the reliability and scientific validity of the experiment. During the daytime, the temperature in the novel roof greenhouse typically exceeded the outdoor temperature by 10–15 °C. This increase can be attributed to the greenhouse's closed design and effective heat collection capabilities. At night, the indoor temperature remained 5–10 °C warmer than the outside, primarily due to the presence of phase change materials (PCMs) within the greenhouse. The PCM absorbs heat during the day and releases it at night, which helps maintain a higher indoor temperature.

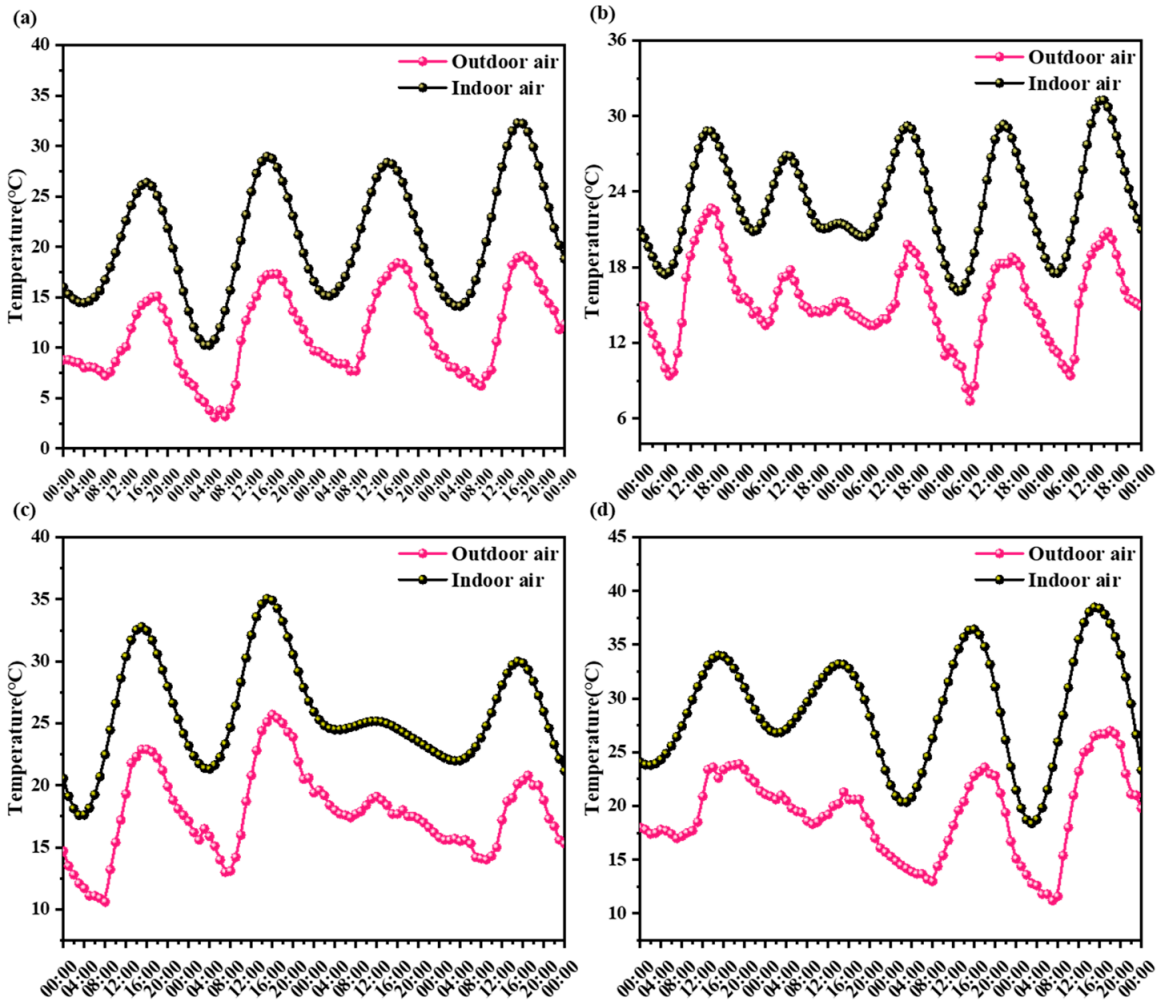


**Figure 12.** The indoor and outdoor temperature changes of the novel rooftop greenhouse during daytime and nighttime from 16 March to 20 March (**a**), 9 April to 13 April (**b**), 29 April to 3 May (**c**), and 12 May to 16 May (**d**).

### *4.3. Growth Analysis of Three Experimental Vegetables*

Based on the measured light and thermal environments, we further conducted plant growth experiments. We purchased three common vegetables as experimental subjects: purslane (P), asparagus (A), and lettuce (L). During the experiment, we recorded the growth of plants in the experimental and control groups from 29 February to 15 May and compared their growth rates and leaf colors (Figure 13a). This experiment aimed to assess the impact of optimized growth conditions in the greenhouse on the growth of different vegetables.

The growth rates of purslane, asparagus, and lettuce in the experimental group were approximately 40%, 30%, and 55% higher than those in the control group, respectively (Figure 13b). Such differences indicate that the optimized growth environment significantly promotes plant growth. In the first phase (from 16 March to 16 April), vegetables were planted for both the experimental and control groups, and their growth was monitored in real time. Through observation, we found that the vegetables in the experimental group not only grew significantly faster but also had a greater number of leaves. This rapid growth phenomenon is likely closely related to the optimized light conditions and temperature control, particularly providing ample sunlight and suitable temperatures during the day, allowing the plants to efficiently carry out photosynthesis.

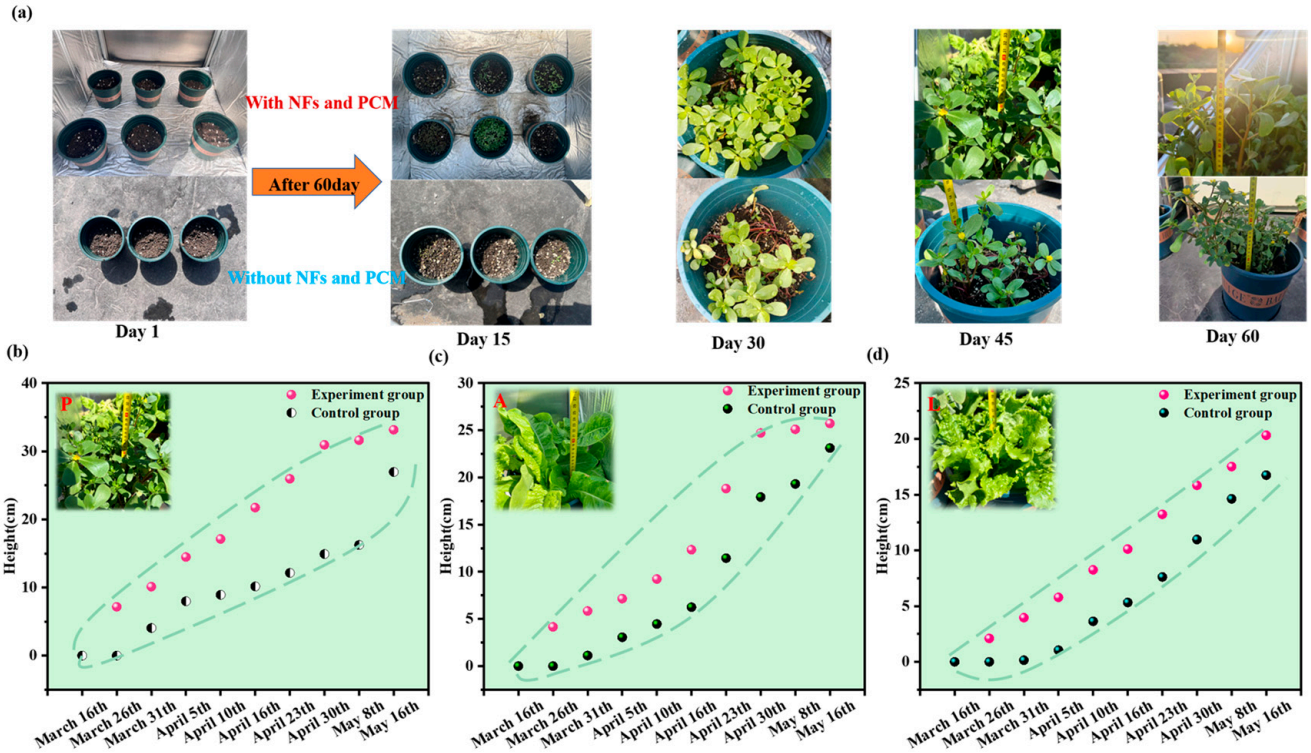


**Figure 13.** Comparison of growth status (**a**) and height of purslane (**b**), asparagus (**c**), and lettuce (**d**) between experimental and control groups.

In the second phase (from 16 April to 16 May), to ensure the normal growth of the vegetables, they were separated and replanted. Specifically, the vegetables from the experimental and control groups were transplanted into different planting areas to better observe and record their growth conditions. The monitoring results indicated that the leaves of the experimental group outperformed those of the control group in terms of color and brightness. The leaves in the experimental group exhibited a fuller green hue, with higher gloss and vitality. Such color changes reflect the health and nutritional levels of the plants; the more vibrant the leaf color, the higher the efficiency of photosynthesis and the richer the accumulation of nutrients. Observations revealed that the color variation in the

leaves of the experimental group was more uniform, resulting in a consistent overall tone, which indicates that the plants had better environmental adaptability during the growth.

Vegetables, as natural energy converters, transform solar energy into chemical energy through photosynthesis, providing essential nutrients for the human body. In the experimental group, purslane and lettuce demonstrated significant advantages in energy accumulation due to the optimized photosynthesis environment of the greenhouse (Figure 14a,b). The greenhouse effectively captured sunlight in the 300–800 nm range, which is the most effective wavelength range for plants to conduct photosynthesis. At the same time, the internal temperature of the greenhouse was precisely controlled within an ideal daytime range of 15–30 °C, providing favorable thermal conditions for photosynthesis.

During the night, the temperature was maintained at 15–18 °C, which not only prevented the plants from suffering damage due to cold conditions but also effectively minimized energy loss. In contrast, the control group's management in this regard was insufficient, leading to slower growth and lower photosynthesis efficiency. The stable environmental conditions resulted in faster growth and more luxuriant foliage in the experimental group, allowing for greater energy accumulation and an overall improvement in growth quality. In terms of nutritional content, the purslane and amaranth in the experimental group showed similar carbohydrate levels, but their protein content was significantly higher due to the optimized growth conditions. This increase in protein was a result of the enhanced photosynthesis occurring under adequate light and suitable temperatures. Additionally, the efficient light spectrum and temperature control during the day maximized photosynthesis and facilitated the plants' absorption and utilization of nutrients. The nighttime temperature regulation further prevented energy loss (Figure 14c).

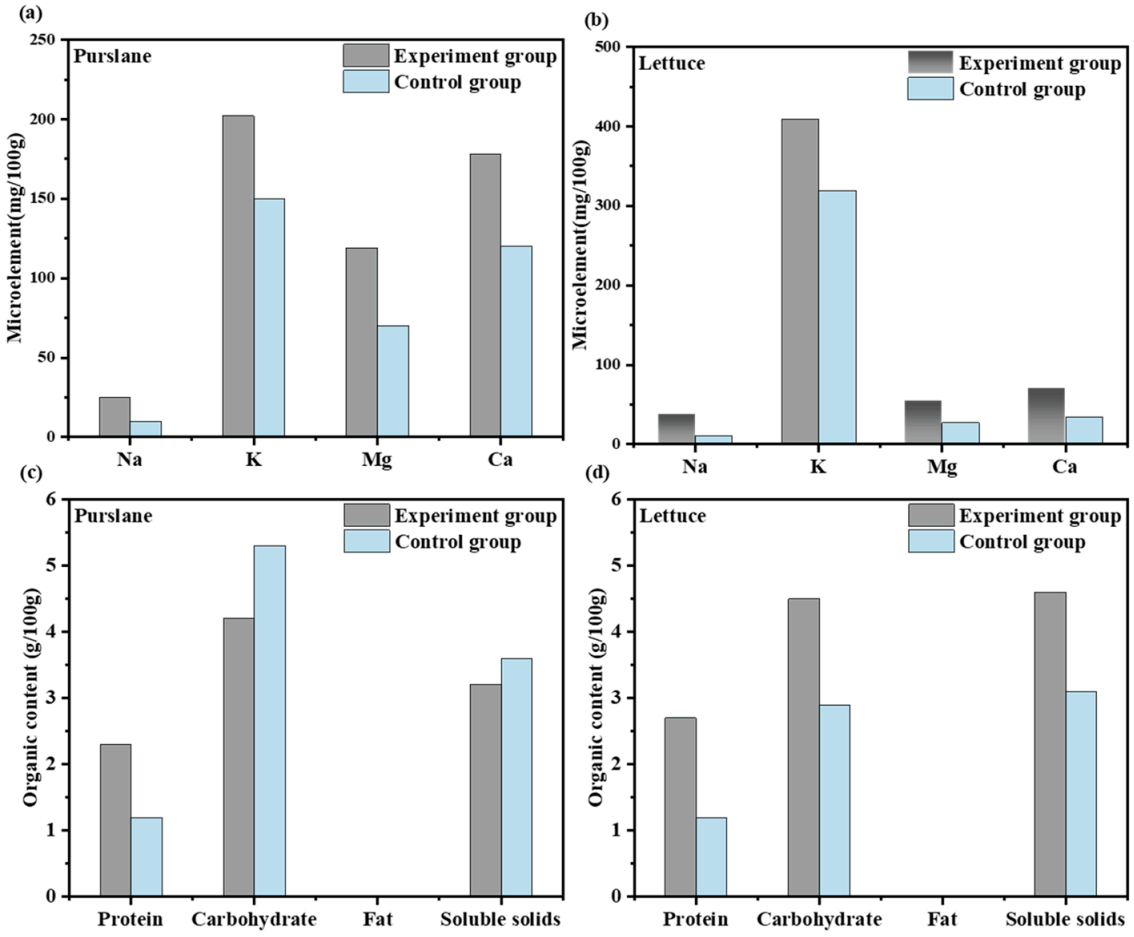


**Figure 14.** The content of trace elements of purslane (**a**) and lettuce (**b**) and the organic content of purslane (**c**) and lettuce (**d**) in vegetables of the experimental and control groups.

This balanced environmental condition promoted the accumulation of proteins and carbohydrates, resulting in higher nutritional value for the vegetables in the experimental group, all while maintaining zero fat content, which further enhanced their health benefits. Furthermore, the higher soluble solid content in the experimental group indicated better nutritional quality.

The fresh weights of roots, stems, and leaves in the experimental group were significantly higher than those in the control group, thanks to an optimized growth environment (Figure 15b). This environment provided well-regulated water management and ideal lighting conditions, which enhanced photosynthesis and transpiration. The controlled temperatures, maintained at 15–30 °C during the day and 15–18 °C at night, promoted effective water absorption and nutrient uptake, contributing to the increased fresh weight. Additionally, the dry weights of roots, stems, and leaves were also higher in the experimental group (Figure 15c). This improvement can be attributed to the application of phase change material technology, which maintained stable temperatures by absorbing heat during the day and releasing it at night. This stability prevented stress on the plants due to temperature fluctuations. The nanofluid lighting system further enhanced photosynthesis by providing an optimal light spectrum (300–800 nm), ensuring better light absorption and increasing the accumulation of organic matter. As a result, the dry weight ratios of roots, stems, and leaves were significantly superior in the experimental group (Figure 15d). The consistent lighting and optimal temperature control contributed to enhanced photosynthesis and nutrient utilization, leading to higher dry weights in the vegetables grown in the experimental group.

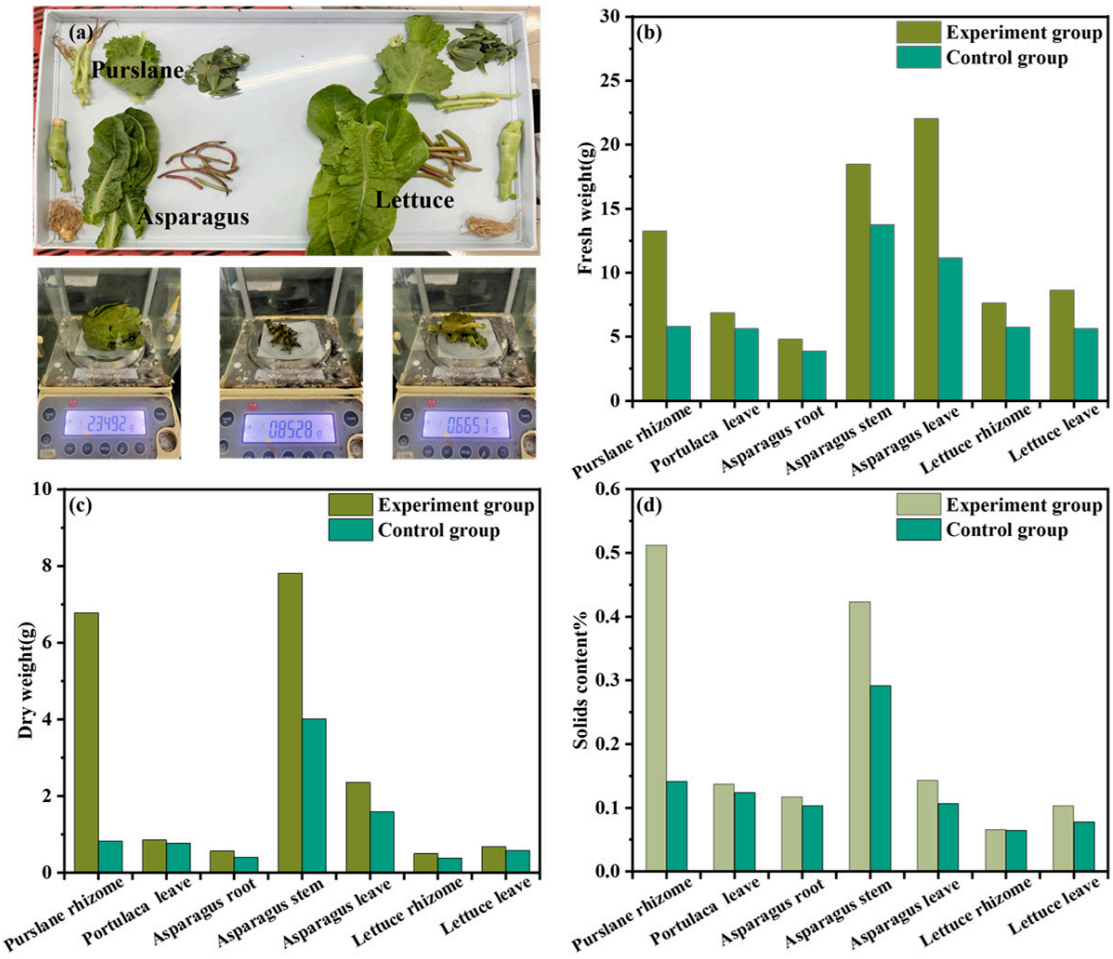


**Figure 15.** Experimental diagram of each part of the vegetable (**a**) and comparison of fresh weight (**b**), dry weight (**c**), and solid content (**d**) of each part of vegetables in the experimental and control groups.

Furthermore, compared to Zhao's study [50], our system provides a longer and more stable temperature range, with higher temperature control precision, creating a more comfortable environment for plant growth and promoting healthier development. Compared to Yuan's study [16], our system shows a clear advantage in thermal efficiency, effectively optimizing energy usage, reducing energy consumption, and improving the overall economic and sustainability performance of the system. Compared to Han's study [51], our cultivated vegetables exhibited superior growth speed and greener leaves, indicating that our system provides more favorable conditions in terms of light, temperature, and humidity, which in turn promotes healthier plant development. Through these comparisons, our research demonstrates significant advantages in temperature control, energy efficiency, and plant growth promotion, strongly highlighting the innovation and uniqueness of our work.

## 5. Conclusions

This paper describes a solar greenhouse system based on nanofluid spectral splitting (NSS) covering applied to the greenhouse roof and phase change materials (PCMs) positioned on the back of the wall to achieve crop production and energy collection for nighttime insulation (solar greenhouse with NSS-PCMs). The main conclusions of this study can be summarized as follows:

(1) The solar roof greenhouse with NSS-PCMs effectively regulated temperature, reducing indoor air temperatures by 3.8 °C during the day and increasing them by 5.6 °C during nighttime. Over 80% of the 300–800 nm light spectrum, optimal for vegetable photosynthesis, was transmitted into the greenhouse, while the remaining wavelengths were absorbed for heat storage, providing warmth during the night.

(2) By optimizing the phase transition temperature (18 °C, 20 °C, and 22 °C) and phase change thickness (2 cm, 3 cm, and 4 cm), the heat absorption and storage capacity were improved, heat release time was extended, and temperature fluctuations were reduced. This enhanced the system's thermal efficiency and photothermal conversion efficiency, stabilized the indoor climate, and provided a more suitable and stable environment for plant growth.

(3) Based on the verified model, the thermal efficiency increased with the phase transition thickness and phase transition temperature of PCMs, with the optimal thickness and temperature of 4 cm and 22 °C. Compared to conventional greenhouses, the optimized solar greenhouse lowered daytime temperatures by 5–6 °C and raised nighttime temperatures by 6.9 °C, ensuring ideal conditions for plant growth throughout the day.

(4) The 75-day temperature detection showed that optimal temperature ranges were maintained for approximately 60 days, both during daytime and nighttime, with an 80% assurance rate.

(5) The growth rates of purslane, asparagus, and lettuce in the experimental group increased by 55%, 35%, and 40%, respectively. The leaves were notably greener, glossier, and more vibrant compared to the control group. In terms of trace elements, the purslane from the experimental group contained 2.5, 1.35, 1.7, and 1.49 times more sodium, potassium, magnesium, and calcium, respectively. For lettuce, the trace elements were 3.8, 1.28, 2.01, and 2.06 times higher. Additionally, for the lettuce from the experimental group, protein, carbohydrates, and soluble solids were 2.25, 1.56, and 1.48 times higher than the control group.

This research is of great significance for the supply of fresh food in urban areas, providing a promising solution for urban vegetable production through the integration of traditional greenhouses with rooftop agriculture. However, the system faces limitations such as high initial costs, limited long-term performance data, and dependence on consistent sunlight. Future recommendations include exploring cost-effective materials and

manufacturing processes to reduce initial costs, conducting long-term durability studies, and investigating alternative energy storage options to improve performance during low-sunlight periods.

**Author Contributions:** Conceptualization, W.W. and J.L.; methodology, Y.S.; software, J.L.; validation, Y.S., W.W. and C.Y.; formal analysis, N.L.; investigation, N.L.; resources, C.Y.; data curation, W.W.; writing—original draft preparation, W.W.; writing—review and editing, W.W.; visualization, J.J.; supervision, B.Y.; project administration, B.Y.; funding acquisition, B.Y. All authors have read and agreed to the published version of the manuscript.

**Funding:** This research is supported by the Natural Science Foundation of Jiangsu Province (No. BK20221315) and the National Natural Science Foundation of China (No. 52238004 and No. 52278111).

**Data Availability Statement:** The data presented in this study are available on request from the corresponding author on reasonable request. The data are not publicly available due to privacy policies.

**Conflicts of Interest:** The authors declare no conflict of interest.

## Nomenclature

| | |
|---|---|
| $\alpha$ | spectral absorptivity |
| $\delta$ | thickness, m |
| $\varepsilon$ | spectral emissivity |
| $\lambda$ | heat conductivity coefficient |
| $\mu$ | dynamic viscosity, Pa·s |
| $\rho$ | density, kg/m$^3$ |
| $\sigma$ | Boltzmann's constant, $5.67 \times 10^{-8}$, W·m$^{-2}$·K$^{-4}$ |
| $\tau$ | spectral transmittance |
| $c$ | specific heat capacity, J/kg·K |
| $D_e$ | water pipe diameter, m |
| $E$ | radiation heat transfer, W |
| $H_p$ | enthalpy of PCMs, J·kg$^{-1}$ |
| $H_s$ | critical enthalpy, J·kg$^{-1}$ |
| $L$ | thickness, m |
| $Nu$ | Nusselt number |
| $P_r$ | Prandtl criterion umber |
| $Q_{latent}$ | latent heat of the PCMs, J |
| $Q$ | heat conduction |
| $Q_s$ | apparent heat of phase transition, J |
| $Q_L$ | latent heat of phase change, J |
| $R_e$ | Reynolds number |
| $sin(h)$ | solar hour angle |
| $T$ | temperatures, °C |
| $u_a$ | wind velocity, m/s |

## References

1. Zambrano-Prado, P.; Muñoz-Liesa, J.; Josa, A.; Rieradevall, J.; Alamús, R.; Gasso-Domingo, S.; Gabarrell, X. Assessment of the food-water-energy nexus suitability of rooftops. A methodological remote sensing approach in an urban Mediterranean area. *Sustain. Cities Soc.* **2021**, *75*, 103287. [CrossRef]
2. Alberti, M.A.; Blanco, I.; Vox, G.; Scarascia-Mugnozza, G.; Schettini, E.; da Silva, L.P. The challenge of urban food production and sustainable water use: Current situation and future perspectives of the urban agriculture in Brazil and Italy. *Sustain. Cities Soc.* **2022**, *83*, 103961. [CrossRef]
3. Song, S.; Lim, M.S.; Richards, D.R.; Tan, H.T.W. Utilization of the food provisioning service of urban community gardens: Current status, contributors and their social acceptance in Singapore. *Sustain. Cities Soc.* **2022**, *76*, 103368. [CrossRef]

4. Toboso-Chavero, S.; Montealegre, A.L.; García-Pérez, S.; Sierra-Pérez, J.; Muñoz-Liesa, J.; Durany, X.G.; Villalba, G.; Madrid-López, C. The potential of local food, energy, and water production systems on urban rooftops considering consumption patterns and urban morphology. *Sustain. Cities Soc.* **2023**, *95*, 104599. [CrossRef]
5. Kumar, P.; Debele, S.E.; Khalili, S.; Halios, C.H.; Sahani, J.; Aghamohammadi, N.; Andrade, M.d.F.; Athanassiadou, M.; Bhui, K.; Calvillo, N.; et al. Urban heat mitigation by green and blue infrastructure: Drivers, effectiveness, and future needs. *Innovation* **2024**, *5*, 100588. [CrossRef]
6. Yang, B.-Y.; Zhao, T.; Hu, L.-X.; Browning, M.H.E.M.; Heinrich, J.; Dharmage, S.C.; Jalaludin, B.; Knibbs, L.D.; Liu, X.-X.; Luo, Y.-N.; et al. Greenspace and human health: An umbrella review. *Innovation* **2021**, *2*, 100164. [CrossRef]
7. Ben Amara, H.; Bouadila, S.; Fatnassi, H.; Arici, M.; Allah Guizani, A. Climate assessment of greenhouse equipped with south-oriented PV roofs: An experimental and computational fluid dynamics study. *Sustain. Energy Technol. Assess.* **2021**, *45*, 101100. [CrossRef]
8. Shi, K.; Yu, B.; Ma, J.; Cao, W.; Cui, Y. Impacts of slope climbing of urban expansion on global sustainable development. *Innovation* **2023**, *4*, 100529. [CrossRef]
9. Hawes, J.K.; Goldstein, B.P.; Newell, J.P.; Dorr, E.; Caputo, S.; Fox-Kämper, R.; Grard, B.; Ilieva, R.T.; Fargue-Lelièvre, A.; Poniży, L.; et al. Comparing the carbon footprints of urban and conventional agriculture. *Nat. Cities* **2024**, *1*, 164–173. [CrossRef]
10. Yang, R.; Xu, C.; Zhang, H.; Wang, Z.; Pradhan, P.; Lian, X.; Jiao, L.; Bai, X.; Cui, S.; Hu, Y.; et al. Urban rooftops for food and energy in China. *Nat. Cities* **2024**, *1*, 741–750. [CrossRef]
11. Masilela, C.O. Urban Agriculture. In *The Wiley Blackwell Encyclopedia of Urban and Regional Studies*; John Wiley & Sons: Hoboken, NJ, USA, 2019; pp. 1–8. [CrossRef]
12. Hallett, S.; Hoagland, L.; Toner, E. Urban Agriculture: Environmental, Economic, and Social Perspectives. In *Horticultural Reviews, Volume 44*; Wiley: Hoboken, NJ, USA, 2016; pp. 65–120. [CrossRef]
13. Qiu, J.; Zhao, H.; Chang, N.-B.; Wardropper, C.B.; Campbell, C.; Baggio, J.A.; Guan, Z.; Kohl, P.; Newell, J.; Wu, J. Scale up urban agriculture to leverage transformative food systems change, advance social–ecological resilience and improve sustainability. *Nat. Food* **2024**, *5*, 83–92. [CrossRef]
14. Nie, J.; Xu, J.; Su, H.; Gao, H.; Jia, J.; Guo, T. Optimization of characteristic parameters of rectangular solar chimney adapted to agricultural greenhouses. *Case Stud. Therm. Eng.* **2024**, *54*, 103971. [CrossRef]
15. Hosseini, M.; Shahverdian, M.H.; Sayyaadi, H.; Javadijam, R. Renewable energy supplying strategy for a greenhouse based on the water-energy-economy nexus. *J. Clean. Prod.* **2024**, *457*, 142388. [CrossRef]
16. Yuan, Y.; Ji, Y.; Wang, W.; Shi, D.; Hai, L.; Ma, Q.; Yang, Q.; Xie, Y.; Li, B.; Wu, G.; et al. Balancing energy harvesting and crop production in a nanofluid spectral splitting covering for an active solar greenhouse. *Energy* **2023**, *278*, 127706. [CrossRef]
17. Kumar, C.M.S.; Singh, S.; Gupta, M.K.; Nimdeo, Y.M.; Raushan, R.; Deorankar, A.V.; Kumar, T.M.A.; Rout, P.K.; Chanotiya, C.S.; Pakhale, V.D.; et al. Solar energy: A promising renewable source for meeting energy demand in Indian agriculture applications. *Sustain. Energy Technol. Assess.* **2023**, *55*, 102905. [CrossRef]
18. Joudi, K.A.; Farhan, A.A. Greenhouse heating by solar air heaters on the roof. *Renew. Energy* **2014**, *72*, 406–414. [CrossRef]
19. Deng, L.; Huang, L.; Zhang, Y.; Li, A.; Gao, R.; Zhang, L.; Lei, W. Analytic model for calculation of soil temperature and heat balance of bare soil surface in solar greenhouse. *Sol. Energy* **2023**, *249*, 312–326. [CrossRef]
20. Guo, Y.; Zhao, H.; Zhang, S.; Wang, Y.; Chow, D. Modeling and optimization of environment in agricultural greenhouses for improving cleaner and sustainable crop production. *J. Clean. Prod.* **2021**, *285*, 124843. [CrossRef]
21. Jeong, S.J.; Niu, G.; Zhen, S. Far-red light and temperature interactively regulate plant growth and morphology of lettuce and basil. *Environ. Exp. Bot.* **2024**, *218*, 105589. [CrossRef]
22. Li, Z.; Zhao, W.; Wang, P.; Zhao, S.; Wang, D.; Zhao, X. Evolution of microbial community and the volatilome of fresh-cut chili pepper during storage under different temperature conditions: Correlation of microbiota and volatile organic compounds. *Food Chem.* **2024**, *451*, 139401. [CrossRef]
23. Xue, R.; Zhang, C.; Yan, H.; Disasa, K.N.; Lakhiar, I.A.; Akhlaq, M.; Hameed, M.U.; Li, J.; Ren, J.; Deng, S.; et al. Determination of the optimal frequency and duration of micro-spray patterns for high-temperature environment tomatoes based on the Fuzzy Borda model. *Agric. Water Manag.* **2025**, *307*, 109240. [CrossRef]
24. Ren, S.; Giusti, M.M. The effect of whey protein concentration and preheating temperature on the color and stability of purple corn, grape and black carrot anthocyanins in the presence of ascorbic acid. *Food Res. Int.* **2021**, *144*, 110350. [CrossRef]
25. Zahra Haeri, S.; Khiadani, M.; Ramezanzadeh, B.; Kariman, H.; Zargar, M. Photo-thermal conversion properties of hybrid NH2-MIL-125/TiN/EG nanofluids for solar energy harvesting. *Appl. Therm. Eng.* **2025**, *258*, 124607. [CrossRef]
26. Suresh, C.; Chithambaram, V.; Muthucumaraswamy, R.; Praveenkumar, S.; Saleh, S.M.; Rao, M.C.; Basem, A.; Alawee, W.H.; Majdi, H.S.; Omara, Z.M.; et al. Transformative nanofluid solutions: Elevating solar still performance for enhanced output. *Ain Shams Eng. J.* **2024**, *15*, 103088. [CrossRef]

27. Htwe, Y.Z.N.; Mamat, H. Progress and prospects on stability and thermal properties of surfactant assisted graphene, carbon nanotubes based nanofluid and their hybrid for next-generation thermal management. *J. Mol. Liq.* **2024**, *414*, 126235. [CrossRef]
28. Wen, J.; Li, X.; Chen, W.; Liu, J. Systematical investigation on the solar-thermal conversion performance of TiN plasmonic nanofluids for the direct absorption solar collectors. *Colloids Surf. A Physicochem. Eng. Asp.* **2021**, *624*, 126837. [CrossRef]
29. Menbari, A.; Alemrajabi, A.A.; Rezaei, A. Heat transfer analysis and the effect of CuO/Water nanofluid on direct absorption concentrating solar collector. *Appl. Therm. Eng.* **2016**, *104*, 176–183. [CrossRef]
30. Babar, H.; Wu, H.; Zhang, W.; Xie, Y. Harnessing nano-synergy: A comprehensive study of thermophysical characteristics of silver, beryllium oxide, and silicon carbide in hybrid nanofluid formulations. *J. Mol. Liq.* **2024**, *414*, 126175. [CrossRef]
31. Mukherjee, S.; Mishra, P.C.; Chaudhuri, P. Stability of Heat Transfer Nanofluids—A Review. *ChemBioEng Rev.* **2018**, *5*, 312–333. [CrossRef]
32. Xu, J.; Chen, B.; Yuan, K.; Shu, J.; Yang, Q. Optimization and performance assessment of Ag@SiO2 core–shell nanofluids for spectral splitting PV/T system: Theoretical and experiment analysis. *Sol. Energy* **2024**, *283*, 113030. [CrossRef]
33. Zhang, G.; Shan, S.; Wu, H.; Tian, J.; Cheng, Z.; Zhou, Z. Investigation on the radiative characteristics of ZnO-SiO2 nanofluids in spectral splitting photovoltaic/thermal systems. *Sol. Energy Mater. Sol. Cells* **2024**, *277*, 113129. [CrossRef]
34. Chougule, S.S.; Srivastava, A.; Bolegave, G.G.; Gaikwad, B.A.; Shirage, P.M.; Markides, C.N. Next-generation solar technologies: Unlocking the potential of Ag-ZnO hybrid nanofluids for enhanced spectral-splitting photovoltaic-thermal systems. *Renew. Energy* **2024**, *236*, 121405. [CrossRef]
35. Subramanian, M.; Hoang, A.T.; Kalidasan, B.; Nižetić, S.; Solomon, J.M.; Balasubramanian, D.; Subramaniyan, C.; Thenmozhi, G.; Metghalchi, H.; Nguyen, X.P. A technical review on composite phase change material based secondary assisted battery thermal management system for electric vehicles. *J. Clean. Prod.* **2021**, *322*, 129079. [CrossRef]
36. Ahmed, S.F.; Rafa, N.; Mehnaz, T.; Ahmed, B.; Islam, N.; Mofijur, M.; Hoang, A.T.; Shafiullah, G. Integration of phase change materials in improving the performance of heating, cooling, and clean energy storage systems: An overview. *J. Clean. Prod.* **2022**, *364*, 132639. [CrossRef]
37. Benli, H.; Durmuş, A. Performance analysis of a latent heat storage system with phase change material for new designed solar collectors in greenhouse heating. *Sol. Energy* **2009**, *83*, 2109–2119. [CrossRef]
38. Bouadila, S.; Kooli, S.; Skouri, S.; Lazaar, M.; Farhat, A. Improvement of the greenhouse climate using a solar air heater with latent storage energy. *Energy* **2014**, *64*, 663–672. [CrossRef]
39. Padash, A.; Shahabivand, S.; Behtash, F.; Aghaee, A. A practicable method for zinc enrichment in lettuce leaves by the endophyte fungus *Piriformospora indica* under increasing zinc supply. *Sci. Hortic.* **2016**, *213*, 367–372. [CrossRef]
40. Zhang, J.; Wang, J.; Zheng, C.; Guo, H.; Shan, F. Nondestructive evaluation of Chinese cabbage quality using mechanical vibration response. *Comput. Electron. Agric.* **2021**, *188*, 106317. [CrossRef]
41. Yu, B.; He, W.; Li, N.; Wang, L.; Cai, J.; Chen, H.; Ji, J.; Xu, G. Experimental and numerical performance analysis of a TC-Trombe wall. *Appl. Energy* **2017**, *206*, 70–82. [CrossRef]
42. Hassan, A.; Abbas, S.; Yousuf, S.; Abbas, F.; Amin, N.M.; Ali, S.; Shahid Mastoi, M. An experimental and numerical study on the impact of various parameters in improving the heat transfer performance characteristics of a water based photovoltaic thermal system. *Renew. Energy* **2023**, *202*, 499–512. [CrossRef]
43. Abbas, S.; Yuan, Y.; Zhou, J.; Hassan, A.; Yu, M.; Yasheng, J. Experimental and analytical analysis of the impact of different base plate materials and design parameters on the performance of the photovoltaic/thermal system. *Renew. Energy* **2022**, *187*, 522–536. [CrossRef]
44. Alsaqoor, S.; Alqatamin, A.; Alahmer, A.; Nan, Z.; Al-Husban, Y.; Jouhara, H. The impact of phase change material on photovoltaic thermal (PVT) systems: A numerical study. *Int. J. Thermofluids* **2023**, *18*, 100365. [CrossRef]
45. Zhou, S.; Bai, F.; Razaqpur, G.; Wang, B. Effect of key parameters on the transient thermal performance of a building envelope with Trombe wall containing phase change material. *Energy Build.* **2023**, *284*, 112879. [CrossRef]
46. Kanzari, I.; Oueslati, H.; Ben Mabrouk, S. Numerical simulation of photovoltaic thermal air panel with phase change materials. *Renew. Energy Focus* **2021**, *37*, 27–35. [CrossRef]
47. Bahaidarah, H.; Subhan, A.; Gandhidasan, P.; Rehman, S. Performance evaluation of a PV (photovoltaic) module by back surface water cooling for hot climatic conditions. *Energy* **2013**, *59*, 445–453. [CrossRef]
48. Gu, Z.; Liu, H.; Li, Y. Thermal energy recovery of air conditioning system—-heat recovery system calculation and phase change materials development. *Appl. Therm. Eng.* **2004**, *24*, 2511–2526. [CrossRef]
49. Oliveira, A.V.S.; Avrit, A.; Gradeck, M. Thermocouple response time estimation and temperature signal correction for an accurate heat flux calculation in inverse heat conduction problems. *Int. J. Heat Mass Transf.* **2022**, *185*, 122398. [CrossRef]

50. Zhao, L.; Shui, Z.; Liu, X.; Yang, T.; Duan, G. Computer-aiding evaluation of north wall effects of a solar greenhouse: Multiphysics modelling of the indoor environment. *Case Stud. Therm. Eng.* **2024**, *64*, 105361. [CrossRef]
51. Han, F.; Chen, C.; Chen, H.; Duan, S.; Lu, B.; Jiao, Y.; Li, G. Research on creating the indoor thermal environment of the solar greenhouse based on the solar thermal storage and release characteristics of its north wall. *Appl. Therm. Eng.* **2024**, *241*, 122348. [CrossRef]